

Optimal properties of porous materials and non-wetting liquids for nanotriboelectrification maximization during intrusion-extrusion process

ELECTRO-INTRUSION PROJECT

HORIZON 2020 | FETPROACT-EIC-07-2020
FET Proactive: Emerging paradigms and communities

GRANT AGREEMENT No. 101017858

Deliverable No.	D2.1	
Deliverable Title	OPTIMAL PROPERTIES OF POROUS MATERIALS AND NON-WETTING LIQUIDS FOR NANOTRIBOELECTRIFICATION MAXIMIZATION DURING INTRUSION-EXTRUSION PROCESS	
Due Date	31.12.2024	
Deliverable Type	Report	
Dissemination level	Public	
Written by	Luis Bartolomé, Yaroslav Grosu, Simone Meloni	11.10.2024
Approved by	General Assembly	16.12.2024
Status	Final	18.12.2024

REVISION HISTORY

Version	Date	Author	Partner	Changes
1	11.10.2024	LUIS BARTOLOMÉ	CICe	1st version

TABLE OF CONTENTS

REVISION HISTORY	2
LIST OF TABLES AND FIGURES	4
LIST OF ABBREVIATIONS.....	9
PROJECT ABSTRACT.....	11
1. EXECUTIVE SUMMARY	12
2. DEVELOPMENT OF PMs FOR INTRUSION/EXTRUSION OF NON-WETTING LIQUIDS (NWLs) 13	
2.1. GRAFTING SILICA POWDERS	13
2.2. CONDUCTIVE NANOPOROUS MONOLITHS.....	19
2.3. HYDROPHOBIC METAL ORGANIC FRAMEWORKS (MOFs)	21
3. NANOTRIBOELECTRIFICATION DURING INTRUSION–EXTRUSION	26
3.1. EXPERIMENTAL SETUP FOR NANOTRIBOELECTRIFICATION	26
3.2. NANOTRIBOELECTRIFICATION EXPERIMENTAL STUDY DURING INTRUSION– EXTRUSION.....	27
3.2.1. ACTIVE CONFIGURATION	28
3.2.2. PASSIVE CONFIGURATION.....	32
3.2.3. MONOLITH CONFIGURATION	39
3.2.4. OTHER CONFIGURATIONS.....	43
3.2.5. SUMMARY OF RESULTS.....	47
4. DEVELOPMENT AND VALIDATION OF NANOTRIBOELECTRIFICATION MODEL.....	49
4.1. MODEL OF NANOTRIBOELECTRIFICATION VIA ELECTRONIC CHARGE TRANSFER.....	51
4.1.1. {ZIF-8 + H ₂ O} CASE.....	51
4.1.2. {GRAFTED SILICA + H ₂ O} CASE.....	54
4.2. MODEL OF NANOTRIBOELECTRIFICATION VIA IONIC CHARGE TRANSFER.....	56
5. CONCLUSIONS	58
6. REFERENCES	60

LIST OF TABLES AND FIGURES

Table 1.- Intrusion pressure and intrusion volume for the optimal batches, <i>i.e.</i> FG150-EA13, -EA14 and -EA15, in comparison to previous hydrophobization attempts, <i>e.g.</i> FG150-EA8 and -EA11.	16
Table 2.- Peaks amplitudes for different materials using 22 K Ω	38
Table 3.- Comparison of different nano-tribogenerators and their power generation.	48
Table 4.- Charge accumulated on pristine and defected ZIF-8. Two values of the lattice parameters have been considered, 17.004 Å, the equilibrium value for the empty system, and 17.064 Å, the value after the 0.06 Å expansion upon intrusion.	53
Table 5.- Charge transfer calculated between the fully-grafted SiO ₂ and water molecules, further broken down into charge transfer between water molecules and the C8-CH ₃ /C8-CF ₃ chain and SiO ₂ surface components via atom-in-molecule partitioning (Bader charges). One notes a directional shift in charge transfer direction driven by the chains.	55
Figure 1.- (a) Pristine silica G150 where a drop of water is infused on it (the drop cannot be observed as it is fully adsorbed) and (b) grafted G150 where the developed hydrophobicity is observed.	13
Figure 2.- Comparison of the intrusion volume depending on the compression-decompression cycle for both grafted silicas FG60 and FG150.	14
Figure 3.- Wettability test of 8 th batch of grafted CF ₃ -SiO ₂ (FG150-EA8) by means of contact angle measurements.	14
Figure 4.- H ₂ O intrusion–extrusion <i>PV</i> -isotherms at (a) room temperature and at (b) 80 °C of batch FG150-EA8. Several intrusion–extrusion cycles were obtained in order to check the stability of the material.	14
Figure 5.- H ₂ O intrusion–extrusion <i>PV</i> -isotherms at room temperature of batch FG150-EA11. This time, stability was improved compared to previous batches but intrusion volume was reduced.	15
Figure 6.- (a) H ₂ O intrusion–extrusion <i>PV</i> -isotherms of the first intrusion–extrusion cycles of different batches. (b) Wettability test of 13 th batch of grafted CF ₃ -SiO ₂ (FG150-EA13), as one of the optimal samples.	15
Figure 7.- H ₂ O intrusion–extrusion <i>PV</i> -isotherms room temperature of (a) the optimal batch 13 where steady intrusion–extrusion behaviour is observed and (b) the three optimal batches synthesized using the same grafting protocol.	16
Figure 8.- FTIR spectra of the optimal batches (FG150-EA13, -EA14 and -EA15) compared to bare commercial G150 silica.	16
Figure 9.- (a) N ₂ -isotherms at 77 K and (b) pore size distribution of the three optimal batches (FG150-EA13, -EA14 and -EA15) compared to reference commercial grafted SiO ₂ (WC8).	17
Figure 10.- SEM images of 13 th batch at different augmentations.	17
Figure 11.- (a) Thermogravimetric decomposition curves of 13 th , 14 th and 15 th batches compared to commercial bare G150 silica. Different mass loss final values represent different grafting densities. In addition, in the 13 th and 15 th batches, two mass-loss steps are clearly seen. The first one at 200 °C is related to non-covalently attached PFOTES molecules. (b) NMR spectra of 13 th , 14 th and 15 th batches. Signals T2 and T3 confirm the covalently bonded PFOTES to the SiO ₂ surface. These spectra also confirm that batch 14 th is the one with less grafted PFOTES.	17

Figure 12.- H ₂ O intrusion–extrusion <i>PV</i> -isotherms of different batches of grafted silica synthesised for the shock absorber prototype (a) for 13 th , 15 th and 17 th batches and (b) for 17 th , 21 st , 23 rd , 25 th and 26 th batches.....	18
Figure 13.- H ₂ O intrusion–extrusion <i>PV</i> -isotherms of the four additional batches of grafted silica with different grafting densities to be not included in the prototype.....	18
Figure 14.- (a) Pristine KIT-6 where a drop of water is infused into it and (b) functionalized KIT-6 where the developed hydrophobicity is observed.	19
Figure 15.- <i>PV</i> -isotherms of a compression-decompression cycle for the KIT-6 functionalized with TCPFOS where no intrusion/extrusion is found.....	19
Figure 16.- Schematic process of the development of superhydrophobic Si monolith.....	20
Figure 17.- (a) Monolith I before hydrophobization and (b) contact angle measurements of monolith I before and after grafting of both sides of the monolith.	21
Figure 18.- XRD of different ZIF-67 qualities, ZIF-L-Co synthesized sample, theoretical model of ZIF-67 and orthorhombic ZIF-L-Co.	21
Figure 19.- <i>PV</i> -isotherms of (a) ZIF-67 HQ, (b) ZIF-67 MQ and (c) ZIF-67 LQ. (d) Evolution of V_{int} and V_{ext} during successive cycles of ZIF-67 HQ, ZIF-67 MQ and ZIF-67 LQ.	22
Figure 20.- Evolution of V_{int} and V_{ext} during successive cycles of ZIF-8 HQ, ZIF-8 MQ and ZIF-8 LQ.	23
Figure 21.- Intrusion volume of non-grafted and grafted ZIF-67 depending on the compression-decompression cycle.....	23
Figure 22.- Intrusion volume of the grafted ZIF-67 depending on the compression-decompression cycle with long pauses between them.	24
Figure 23.- Comparison for grafted and non-grafted ZIF-71 of the (a) intrusion–extrusion isotherms of the first compression-decompression cycle and the (b) intrusion volume depending on the compression–decompression cycle.....	24
Figure 24.- (a) <i>PV</i> -isotherms of ZIF-8 (black dashed line), ZIF-67 (red dotted line) and Co/Zn-ZIF (green line). (b) Evolution of V_{int} during successive cycles of ZIF-67 (red line), ZIF-8 (black line) and Co/Zn-ZIF (green line).....	25
Figure 25.- Main parts of the custom-made PVT device: (a) Control and data acquisition, (b) syringe body, (c) hydraulic circuit and (d) electrical circuit.....	26
Figure 26.- (a) The vessel of PVT-device, (b) the lid to close the vessel and to pass through wires, (c) rupture disc to limit the maximum pressure in the system and (d) the heat exchanger for the vessel.....	27
Figure 27.- Schematic circuits for (a) active configuration, (b) passive configuration and (c) monolith configuration.	27
Figure 28.- Schematic circuit for the double-electrode passive configuration where the porous material is only touching one electrode.	28
Figure 29.- 3D-printed cell, electrodes and spacers to be connected electrically and insulated by silicone for the double-electrode active configuration.....	28
Figure 30.- Electrical signal (orange line) and pressure (blue line) of a compression–decompression test at 0.2 ml/s for the double-electrode active configuration.....	29
Figure 31.- Electrical power (orange line) of a compression/decompression test at 0.2 ml/s for the double-electrode active configuration and the corresponding generated energy calculated by integration.	29
Figure 32.- Effect of the applied bias voltage on the generated electrical energy and power density for the double-electrode active configuration using a distance between the electrodes of 5.2 mm. $R=100 \Omega$	29

Figure 33.- Effect of the applied bias voltage in the generated electrical energy and power density for the double-electrode active configuration using a distance between electrodes of 1.77 mm. $R=100 \Omega$	30
Figure 34.- Intrusion isotherms of grafted silica C8-CH ₃ for the double-electrode active configuration. It can be noted between cycle 27 and cycle 28 the intrusion volume decreases due to the system being, between these two cycles, under 4 V for almost 12 h.....	31
Figure 35.- Voltage signal for three compression/decompression cycles (a) before and (b) after applying bias voltages for the double-electrode passive configuration.	31
Figure 36.- (a) Current and (b) voltage during a compression/decompression cycle for the double-electrode active configuration with an applied bias voltage of 0.5 V.	31
Figure 37.- Results of three compression-decompression cycles for the double-electrode passive configuration, along with magnifications of a single cycle and its corresponding intrusion.....	32
Figure 38.- Parameters to study electrification for the double-electrode passive configuration: (a) maximum current and (b) energy.....	33
Figure 39.- Maximum current at intrusion and extrusion depending on the compression/decompression rate.	33
Figure 40.- Generated energy at intrusion and extrusion depending on the compression/decompression rate.	33
Figure 41.- Vessel of PVT-device with the heat exchanger and the thermal insulation to carry out experimental tests at 5.5 °C.....	34
Figure 42.- Maximum current at intrusion and extrusion into and from C8-CH ₃ depending on the compression/decompression rate comparing room temperature and 5.5 °C.	34
Figure 43.- Generated electrical energy during intrusion and extrusion of water into and from C8-CH ₃ depending on the compression/decompression rate at room temperature and 5.5 °C.	34
Figure 44.- Parameters to optimize the electrical resistance for the double-electrode passive configuration: (a) current and (b) voltage amplitudes.	35
Figure 45.- (a) Current and voltage amplitudes and (b) power density at different electrical resistances in the circuit of the double-electrode passive configuration with the system {H ₂ O + C8-CH ₃ }.	35
Figure 46.- (a) Voltage signal for 10 compression–decompression cycles with a waiting time of 1 s and (b) power density depending on the compression–decompression cycle at different waiting times.....	36
Figure 47.- (a) Current and (b) voltage during a compression–decompression cycle for the double-electrode passive configuration with MOF ZIF-8.....	36
Figure 48.- (a) Current and voltage amplitudes and (b) power density at different electrical resistances in the circuit of the double-electrode passive configuration with MOF ZIF-8.	36
Figure 49.- Generated electrical energy per cycle during intrusion-extrusion of water into-from (a) MOF ZIF-8 and (b) grafted C8-CH ₃ silica for the double-electrode passive configuration.	37
Figure 50.- Generated electrical energy per cycle during intrusion-extrusion of different liquids into-from MOF ZIF-8 for the double-electrode passive configuration.	37
Figure 51.- Generated electrical energy per cycle during intrusion-extrusion of different liquids into-from MOF ZIF-8 for the double-electrode passive configuration.	38
Figure 52.- (a) Voltage signal during 147 cycles at 0.075 Hz. (b) Voltage peak amplitude progression with the cycles, an average of 20 cycles.	39
Figure 53.- Progression of the generated energy per intrusion-extrusion cycle for different materials and configurations.	39
Figure 54.- Pore size and porous layer thickness of the three samples of Si-monolith.....	39

Figure 55.- Circuit connections for the monolith configuration: (a) monolith connected to positive terminal del ammeter and then ground, (b) monolith connected to positive terminal del ammeter and then metallic vessel, (c) monolith connected to negative terminal del ammeter and then ground and (d) monolith connected to negative terminal del ammeter and then metallic vessel.....	40
Figure 56.- Generated energy per intrusion-extrusion cycle for different circuit connections for the monolith configuration with sample II.	40
Figure 57.- Electrical signal (orange line) and pressure (blue line) of a compression–decompression test at $0.005 \text{ ml}\cdot\text{s}^{-1}$ for the monolith configuration of (a) sample 0, (b) sample I and (c) sample II.	40
Figure 58.- (a) Voltage and (b) current signal with the peaks of intrusion/extrusion and pressure of a compression/decompression test at $0.3 \text{ ml}\cdot\text{s}^{-1}$ for sample 0 with the monolith configuration.	41
Figure 59.- (a) Current and voltage amplitudes and (b) power density at different electrical resistances in the circuit of the monolith configuration with sample 0.	41
Figure 60.- Generated energy per intrusion-extrusion cycle for different Si-monolith samples at different electrical resistances.	41
Figure 61.- Generated energy per intrusion-extrusion cycle for Si monolith sample 0 at different compression/decompression rates.....	42
Figure 62.- (a) Si-monolith encapsulated and (b) schematic circuit for the encapsulated Si-monolith configuration.	42
Figure 63.- Voltage during compression–decompression cycles for the encapsulated Si-monolith configuration with (a) water, (b) heavy water and (c) PEI solution.....	42
Figure 64.- (a) Power density and (b) energy per cycle for the encapsulated Si-monolith configuration with water, heavy water and PEI solution.....	43
Figure 65.- Schematic circuit for the single–electrode passive configuration using a Cu-porous electrode and grafted silica C8-CH ₃ as porous material.....	43
Figure 66.- (a) Porous-copper strip used as electrode and (b) how it was wrapped in PTFE tape and connected to the circuit.	43
Figure 67.- Electrical signal (orange line) and pressure (blue line) of a compression/decompression test at 0.02 ml/s for the single–electrode passive configuration using a Cu-porous electrode.	44
Figure 68.- Schematic circuit for the single–electrode passive configuration using a Cu-porous electrode and ZIF-8 as porous material.	44
Figure 69.- Schematic circuit for the single–electrode passive configuration using a coated Cu-film electrode.	44
Figure 70.- (a) C8-CH ₃ -coated copper film used as electrode and (b) connection to the circuit.....	45
Figure 71.- (a) Intrusion/extrusion isotherms of C8-CH ₃ -coated copper film and (b) intrusion/extrusion isotherms of raw grafted silica C8-CH ₃	45
Figure 72.- Electrical signal (orange line) and pressure (blue line) of a compression/decompression test at 0.02 ml/s for the single–electrode passive configuration using C8-CH ₃ -coated Cu-film electrode. No electrification was observed during intrusion-extrusion cycling.....	45
Figure 73.- SEM images of the C8-CH ₃ -coated copper film where the migration of the cover polymer is observed.....	46
Figure 74.- Schematic circuit a configuration using oil to insulate the porous material and the film electrode inside a glass bottle.	46

Figure 75.- Electrical signal (orange line) and pressure (blue line) of a compression/decompression test at $0.3 \text{ ml}\cdot\text{s}^{-1}$ rate for the oil configuration. No electrification was observed during intrusion–extrusion process.	46
Figure 76.- Schematic circuits (a) with the counter electrode outside of the measuring vessel and (b) alternative connection to the log circuit.	47
Figure 77.- Electrical signal (orange line) and pressure (blue line) of a compression/decompression test at $0.3 \text{ ml}\cdot\text{s}^{-1}$ rate for the double-electrode passive configuration using an external counter electrode. No electrification was observed during intrusion-extrusion cycling.	47
Figure 78.- Progression of the power density per intrusion-extrusion cycle for different materials and configurations.	48
Figure 79.- Scheme of the mechanism of contact electrification between two dielectrics before contact (left), in contact (centre) and after contact (right), illustrating electron transfer in the instance that dielectric B's acceptor level potential is lower than the donor level of dielectric A. Similar schemes hold for dielectrics in contact with molecular systems, <i>e.g.</i> liquids ¹⁷	49
Figure 80.- Cartoon illustrating the calculations to determine electronic charge transfer via the difference of electronic density of the entire system (left) and solid (centre) and liquid (right) subsystems sampled by molecular dynamics.	51
Figure 81.- Density of states of VZn'' ZIF-8 (purple) and bulk water (green). The ZIF-8 gap states are in close proximity to those of the bulk water acceptor states. This contrasts with perfect and $VIm \bullet$, which have no bandgap states.	52
Figure 82.- Plot of the density variation $\Delta\rho$ showing that excess charge (of opposite sign) is localized on the framework and an individual water molecule laying in a pseudo-hexagonal window connecting neighbouring ZIF-8 cavities.	53
Figure 83.- Visualisation of charge differences calculated for (a) C8-CH ₃ and (b) C8-CF ₃ when solvated in H ₂ O (yellow represents charge gain and blue charge loss. Isolvalue 0.001). This graphic illustrates strong differences between the C8-CH ₃ and C8-CF ₃ chains alluded to in the text. C8 chains are highly flexible and fold to cover the SiO ₂ surface, preventing SiO ₂ surface–water contact. C8-CF ₃ chains are increasingly rigid, leaving larger uncovered gaps between grafting chains, allowing contact between water and the silica surface, in a range in which charge transfer can occur.	54
Figure 84.- Density of states (DOS) for C8-CH ₃ (left) and C8-CF ₃ (right) grafted silica. In red are reported DOSs of the solid and in cyan the ones of water. In the first row, panel (a) we report data for pristine grafted silica. In panel (b) data are reported for a grafting defect obtained by removing a Si ⁺ terminated chain. In panel (c) we report corresponding data for a grafting defect corresponding to the removal of a O ⁻ terminated chain.	56
Figure 85.- Schematic outlining the possible mechanism of ionic charge transfer. In the (a) initial step, a (charged) grafting defect is located by removing a (b) O ⁻ terminated or (c) Si ⁺ terminated chain. Our simulations revealed that the detached molecule reorientated, exposing the charged species toward bulk water. In the final step, the charged molecule can take H ⁺ or OH ⁻ from water, depending on the relative acidity of the species.	57

LIST OF ABBREVIATIONS

Acronym / Short name	Meaning
ADC	Analog-to-Digital Converter
BJH	Barret-Joyner-Halenda
C8-CF₃	Fluorinated grafted silica gel C8
C8-CH₃	Hydrogenated grafted silica gel C8
DMF	Dimethylformamide
DOS	Density of states
DSC	Differential Scanning Calorimetry
EXT	Extrusion
FoM	Figure of merit
FTIR	Fourier-transform infrared spectroscopy
HQ	High Quality
INT	Intrusion
LQ	Low Quality
MD	Molecular Dynamics
MOF	Metal-Organic Framework
MQ	Medium Quality
NTE	Nanotriboelectrification
NWL	Non-wetting liquid
PEI	Polyethylenimine
PFOTES	1H,1H,2H,2H-perfluorooctyltriethoxysilane
PM	Porous material
PTFE	Polytetrafluoroethylene (Teflon)
PVDF	Polyvinylidene difluoride
PV	Pressure-volume
PVT	Pressure-volume-temperature
SEM	Scanning electron microscope
TCPFOS	Trichloro (1H,1H,2H,2H-perfluorooctyl) silane
TCTFPS	Trichloro (3,3,3-trifluoropropyl) silane
TENG	Tribo-electric nanogenerator
TGA	Thermogravimetric analysis
WP	Work Package
XRD	X-Ray Diffraction
KIT	Korea Advanced Institute of Science and Technology
V_{ext}	Extrusion volume
SOD	Sodalite

Acronym / Short name	Meaning
P_{int}	Intrusion pressure
P_{ext}	Extrusion pressure
OPLS-AA	Optimized Potentials for Liquid Simulations - All Atom
ZIF	Zeolitic Imidazolate Framework
V_{int}	Intrusion volume

PROJECT ABSTRACT

– Simultaneous transformation of ambient heat and undesired vibrations into electricity via nanotriboelectrification during non-wetting liquid intrusion-extrusion into-from nanopores –

Greenhouse gas emissions, pollution and rational energy use are civilization-scale challenges which need to be resolved urgently, in particular by the conversion of abundant waste heat and undesired vibrations into useful electricity. However, the low efficiency of existing conversion methods does not provide an attractive solution.

Electro-Intrusion project proposes a new and highly efficient method and apparatuses for the simultaneous transformation of mechanical and thermal energies into electricity by using zero-emission nanotriboelectrification during non-wetting liquid intrusion-extrusion into-from nanoporous solids.

To tackle these phenomena, Electro-Intrusion project brings together a consortium of multidisciplinary teams specializing in physics, chemistry, material science and engineering to address the project by the state-of-the-art methods of molecular dynamic simulations, high-pressure calorimetry and dielectric spectroscopy, materials synthesis and characterization, and prototype development. The FET-PROACTIVE call is a key solution to bring this early-stage multidisciplinary concept to higher TRLs, fill in the large knowledge gaps in the solid-liquid contact electrification and heat generation during intrusion-extrusion as well as enable its full impact on EU innovation leadership, competitive market and energy sector security.

The proposed method can be used for energy scavenging within a wide range of technologies, where vibrations and heat are available in excess (train, aviation, domestic devices, drilling, etc.). In particular, using European Environment Agency data, this project estimates that the use of the proposed approach only within the automobile sector can reduce the overall EU electricity consumption by 1-4 % in 2050. With this regard, the final stage of the project implies regenerative shock absorber development and field-testing for a drastic maximization of the maximum range of hybrid / electric vehicles.

Electro-Intrusion project was originally scheduled to run from January 1st, 2021 to December 31st, 2024, for a total duration of 48 months and has received funding from the European Union's H2020 research and innovation programme under grant agreement No. 101017858. A full list of partners and funding can be found at: <https://cordis.europa.eu/project/id/101017858/es>. It has been extended to run till 31st of December 2025.

1. EXECUTIVE SUMMARY

Three parallel activities of this WP are targeting intrusion-extrusion triboelectrification process and include i) synthesis and characterization of porous materials ii) experiments and iii) numerical simulations.

Considerable challenges were evident during the first year of the project, since the materials demonstrated intrusion pressure, which was too high for the final prototype, or exhibited no extrusion or were not stable enough under intrusion-extrusion cycling. Finally, those challenges were resolved. A stable material with required hysteresis for vibrations dumping, stability under intrusion-extrusion cycling and pronounced electrification was synthesised in a quantity required for the prototype. These materials were fully characterized.

To perform the electrification experiments a custom-made setup was developed, calibrated and adjusted for the needs of the project. The experimental campaign started with the active scheme, where bias voltage was applied. This configuration resulted in high values of generated energy with considerably higher Figure of Merit (FoM) compared to the state-of-the-art. However, it was discovered that the bias voltage leads to Porous Materials (PMs) degradation and slow discharge kinetics, so a mitigation strategy was applied by switching to a passive scheme. This strategy resolved both degradation as well as kinetic problems, however lowering the generated energy below expected values. It was found that compression-decompression speed increases the electrification effects, so it is expected that under high-frequency operation of the prototype, the generated energy increases. It was found that triobolary noticeably affects the electrification process, while temperature has a mild effect on it. Moreover, a model like system with controlled current collection and record power density per unit area was achieved. This monolith configuration demonstrates excellent performance even though it is not optimized. The effect of important parameters such as temperature, compression-decompression rate, electrification scheme, grafting nature, particle size and nano-additives was studied.

Simulations have been performed to identify the mechanism of contact electrification between porous solids and intruded liquids. Present theories indicate that liquid/solid triboelectrification in ordinary interface systems is due to electron transfer in/from surface gap states. These states, however, are either absent in the case of the internal surface of crystalline porous materials, like metal-organic frameworks (MOFs), or are expected to not get in direct contact with the liquid in the case of grafted porous systems, like grafted silica. First, we focused on a prototypical hydrophobic MOF, the zeolitic imidazolate framework - ZIF-8, and we have shown that ZIF-8/H₂O contact electrification occurs thanks to the presence of points defects, namely, zinc vacancies. Zinc vacancies can be pre-existing or can be formed upon intrusion. Our calculations show that the peculiar negative compressibility of ZIF-8 upon intrusion may help the formation of this defect beyond its thermodynamic concentration. In particular, following current literature, we first considered the hypothesis that contact electrification is due to electron transfer between the liquid and solid. We have found that the presence of “genuine” defects in MOF and grafting defects in hydrophobized silica surfaces are critical for contact electrification by electronic transfer. We also started investigating contact electrification due to ionic transfer. The investigation of this latter mechanism will be completed in the final part of the project, together with the modelling of contact electrification in the monolithic case.

2. DEVELOPMENT OF PMs FOR INTRUSION/EXTRUSION OF NON-WETTING LIQUIDS (NWLs)

For the development of porous materials to be used in nanotriboelectrification, three main strategies were followed:

1. Grafting silica powders
2. Conductive nanoporous monolith
3. Hydrophobic metal-organic frameworks (MOFs)

2.1. GRAFTING SILICA POWDERS

This strategy is beneficial for minimizing the risks for the development of the planned prototypes because KPI team has profound experience in intrusion-extrusion shock absorbers based on silica powders¹. Both commercial and synthesized porous materials are used for this project.

A commercial nanoporous grafted silica known as Symmetry Prep C8 supplied by WATERS was used, hereinafter referred to as grafted silica C8-CH₃. The grafting was done with octylsilanes with a density of 2.1 groups nm⁻². The average pore size of the material before grafting is 9.2 nm. Nitrogen sorption measurements on the grafted material at 77 K give a porous volume of 0.53 cm³.g⁻¹ and an average pore radius of 4.2 nm, obtained from the desorption branch using the classical Barret-Joyner-Halenda (BJH) equation.

Regarding the functionalization of silicas SiO₂, two silicas with different pore sizes were selected to be grafted by fluorinated groups. The CF₃ group was chosen, as it was proved previously that the CF₃ group demonstrated more pronounced triboelectrification effects with water compared to CH₃ groups². Thus, two commercial silicas from Davisil Grace with average pores of 6 nm (FG60) and 15 nm (FG150) were grafted with CF₃ groups. The grafting protocol for both silicas began weighing 1 g of each silica and washing it with dichloromethane. Then it was dried overnight at 100 °C. After that, the washed silica was dispersed the washed silica in an absolute ethanol/ammonia solution mixture (88 ml/4 ml respectively) under stirring for 30 minutes. Then 0.770 ml of 1H,1H,2H,2H-perfluorooctyltriethoxysilane (PFOTES) were added to this mixture letting stirring for 48 hours. After 2 days, a white precipitate was collected and washed three times with absolute ethanol. Finally, the sample was dried overnight at 70 °C. This fluorinated grafting developed hydrophobicity (Figure 1) in both silicas, this hydrophobic behaviour is due to the decrease in surface free energy by the grafting of CF₃ groups. The study of intrusion/extrusion capacity of these both CF₃-grafted silicas revealed that the intrusion volume decreased after the first cycle and that the complete extrusion was not achieved at atmospheric pressure. Comparing both silicas, the CF₃-grafted silica FG60 showed lower intrusion volume than the grafted FG150. This fact could be due to the pore size of the silicas.

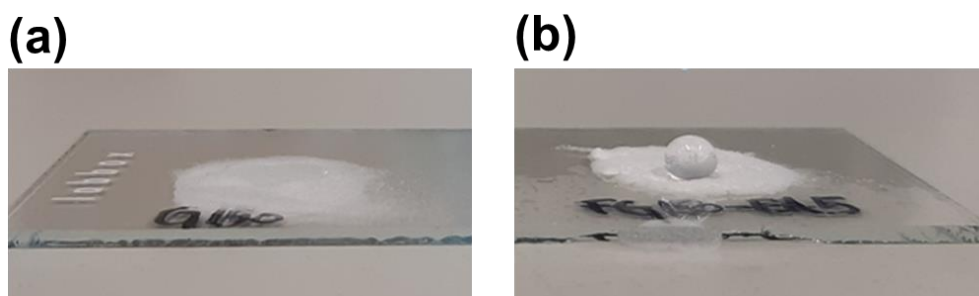


Figure 1.- (a) Pristine silica G150 where a drop of water is infused on it (the drop cannot be observed as it is fully adsorbed) and (b) grafted G150 where the developed hydrophobicity is observed.

The study of intrusion–extrusion capacity of these both CF_3 -grafted silicas revealed that the intrusion volume decreased after the first cycle and that the complete extrusion was not achieved at atmospheric pressure. Comparing both silicas, the CF_3 -grafted silica FG60 showed lower intrusion volume than grafted FG150 (Figure 2). This fact could be due to the pore size of the silicas. The fact that a clear intrusion step was achieved demonstrates that the grafting was successfully applied. However, the protocol must be further improved to reach extrusion process. In some earlier works, it was demonstrated that reaching the extrusion is not trivial for grafted silica³, as topological effects on bubble nucleation are still to be fully understood⁴ and even more so the behavior of long flexible CF_3 chains under the intrusion–extrusion conditions.

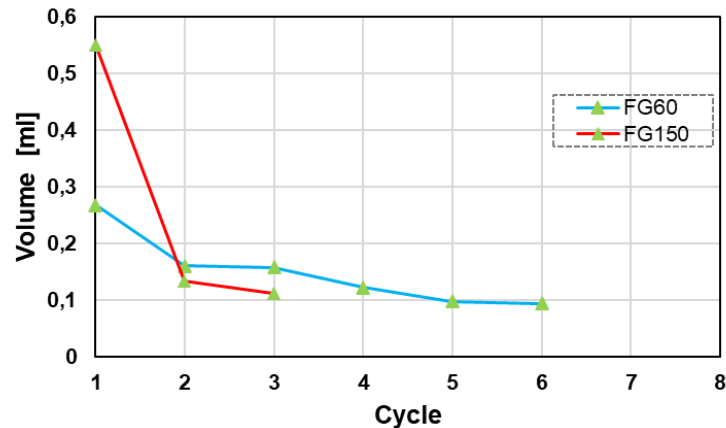


Figure 2.- Comparison of the intrusion volume depending on the compression-decompression cycle for both grafted silicas FG60 and FG150.

As the grafted FG150 was the most promising silica, several hydrophobization attempts were carried out starting from easy protocols involving low-cost solvents and low-temperature-dependent processes to minimize efforts and costs, resulting in superhydrophobic $\text{CF}_3\text{-SiO}_2$ powders (Figure 3).



Figure 3.- Wettability test of 8th batch of grafted $\text{CF}_3\text{-SiO}_2$ (FG150-EA8) by means of contact angle measurements.

Moreover, these grafted $\text{CF}_3\text{-SiO}_2$ silica also exhibit high intrusion pressures (Figure 4).

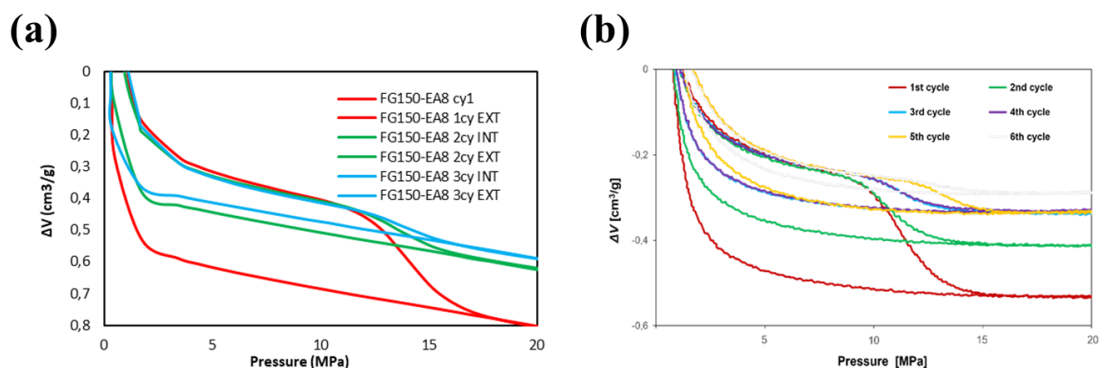


Figure 4.- H_2O intrusion–extrusion PV -isotherms at (a) room temperature and at (b) 80 °C of batch FG150-EA8. Several intrusion–extrusion cycles were obtained in order to check the stability of the material.

As can be seen from comparing the Figure 4 and Figure 5, these attempts did not lead to the desired intrusion–extrusion performances, *i.e.* stability during intrusion–extrusion cycles or hysteresis loop.

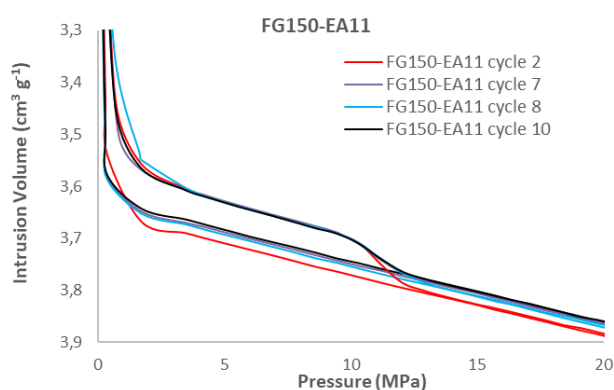


Figure 5.- H₂O intrusion–extrusion PV-isotherms at room temperature of batch FG150-EA11. This time, stability was improved compared to previous batches but intrusion volume was reduced.

So, the grafting conditions were systematically modified one-by-one per batch until the optimal super-hydrophobicity, *i.e.* contact angles higher than 130°, and H₂O intrusion–extrusion performance were achieved (Figure 6).

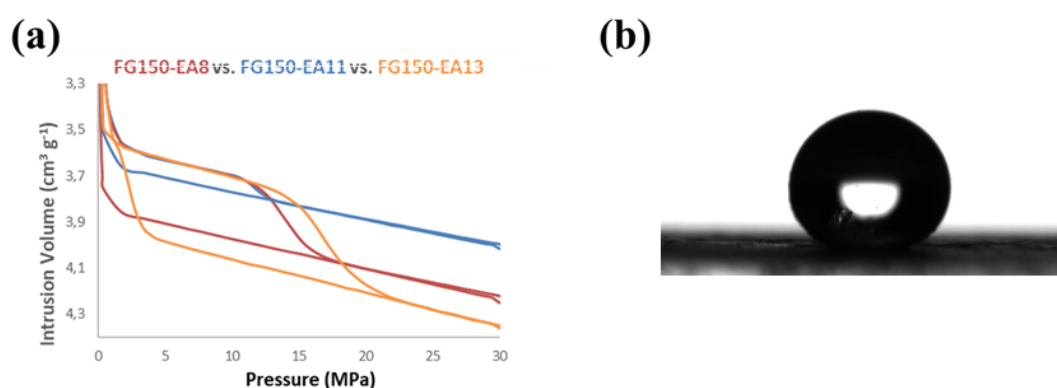


Figure 6.- (a) H₂O intrusion–extrusion PV-isotherms of the first intrusion–extrusion cycles of different batches. (b) Wettability test of 13th batch of grafted CF₃-SiO₂ (FG150-EA13), as one of the optimal samples.

Therefore, the protocol for optimal batches was following:

Firstly, 1 g of GRACE 150 (G150) silica was weighted and washed with dichloromethane. Then it was dried overnight at 120 °C under vacuum. After that, the washed silica was dispersed in an absolute ethanol/ammonia solution mixture (88 ml/4 ml respectively) under stirring for 30 minutes at 50 °C, until proper dispersion was reached. Then 0.55 ml of 1H,1H,2H,2H-perfluorooctyltriethoxysilane (PFOTES) were added dropwise to this mixture letting stirring for 120 hours. After 5 days, a white precipitate was centrifuged and washed three times with absolute ethanol. Finally, the sample was dried overnight at 70 °C. This protocol does not involve highly energetic process or expensive solvents. Our main purpose was from the beginning to obtain an easily reproducible protocol with cheap and abundant solvents and reagents. Through this process three different batches were synthesized in order to check reproducibility (batches 13, 14 and 15 respectively), all superhydrophobic, *i.e.* contact angles higher than 130° (Figure 6b), with good cyclability (Figure 7a) and different intrusion/extrusion pressures depending on grafting density (see Figure 7b and Table 1).

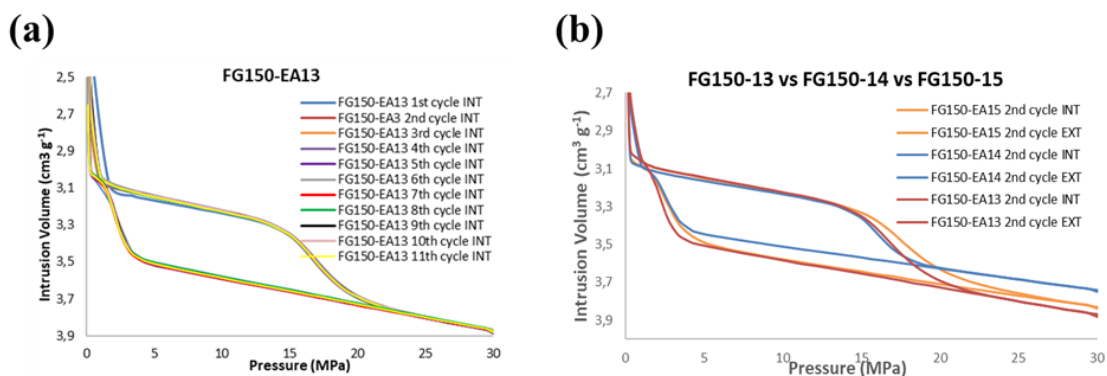


Figure 7.- H₂O intrusion–extrusion PV-isotherms room temperature of (a) the optimal batch 13 where steady intrusion–extrusion behaviour is observed and (b) the three optimal batches synthesized using the same grafting protocol.

Table 1.- Intrusion pressure and intrusion volume for the optimal batches, *i.e.* FG150-EA13, -EA14 and -EA15, in comparison to previous hydrophobization attempts, *e.g.* FG150-EA8 and -EA11.

Material	Intrusion pressure [MPa]	Intrusion volume [cm ³ ·g ⁻¹]
FG150-EA8	13.7	0.09
FG150-EA11	12	0.27
FG150-EA13	16.7	0.315
FG150-EA14	16.5	0.241
FG150-EA15	17.6	0.302

Characterization of the three optimal batches, *i.e.* FG150-EA13, -EA14 and -EA15, was carried out by means of different techniques: infrared spectroscopy (Figure 8) to confirm the correct grafting of the PFOTES.

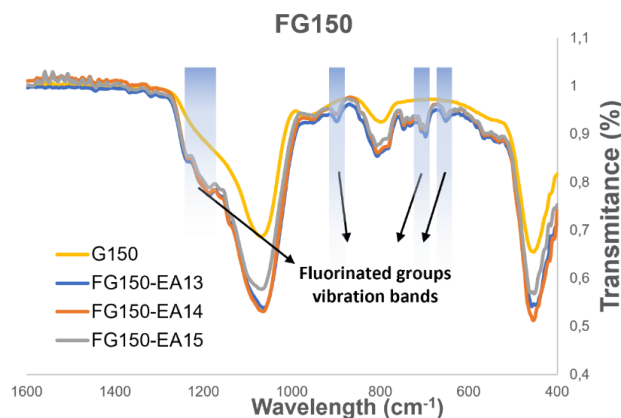


Figure 8.- FTIR spectra of the optimal batches (FG150-EA13, -EA14 and -EA15) compared to bare commercial G150 silica.

To study textural properties, N₂ adsorption at 77 K was also carried out (Figure 9).

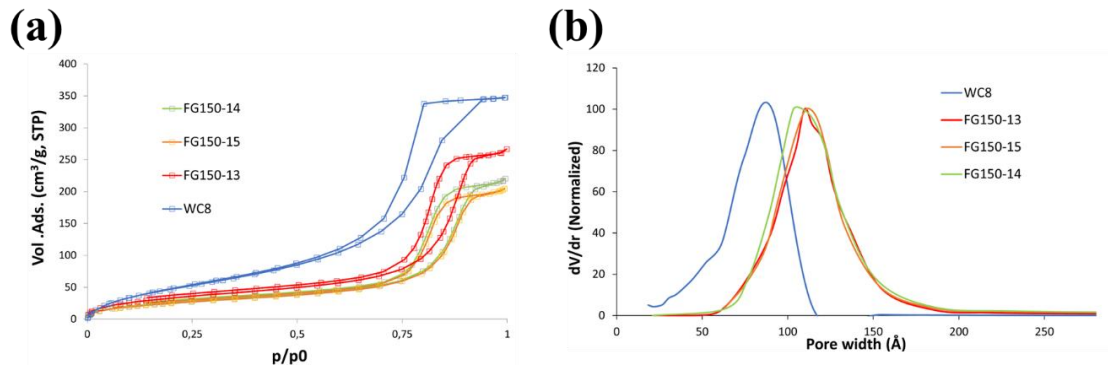


Figure 9.- (a) N₂-isotherms at 77 K and (b) pore size distribution of the three optimal batches (FG150-EA13, -EA14 and -EA15) compared to reference commercial grafted SiO₂ (WC8).

To check particle size, elemental composition and porosity electron microscopy were carried out (Figure 10).

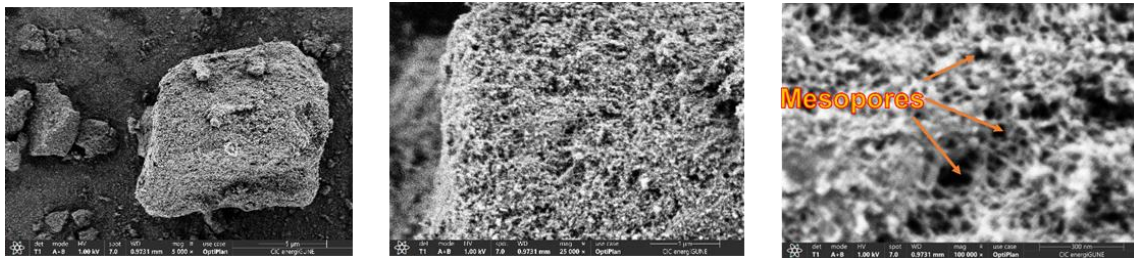


Figure 10.- SEM images of 13th batch at different augmentations.

Finally, thermogravimetric analysis was also carried out (Figure 11a) to check the grafting density by mass and nuclear magnetic resonance (Figure 11b) to confirm the covalent bonding of the PFOTES and qualitatively check the grafting density differences between the three samples.

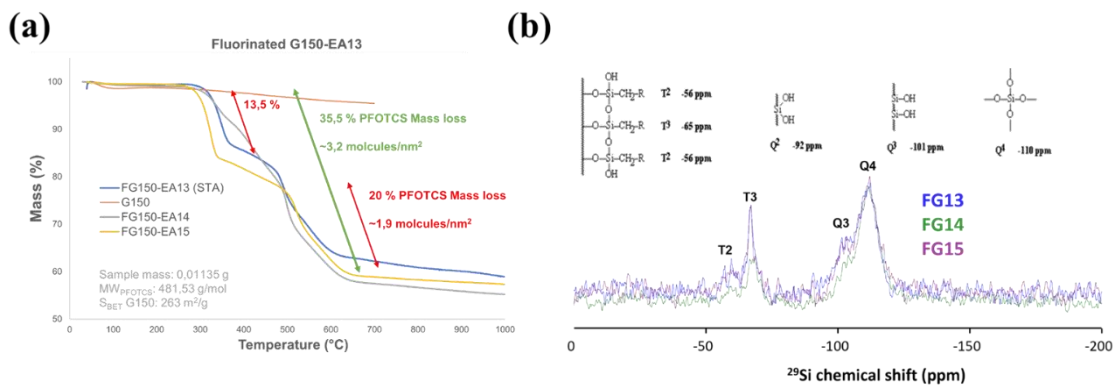


Figure 11.- (a) Thermogravimetric decomposition curves of 13th, 14th and 15th batches compared to commercial bare G150 silica. Different mass loss final values represent different grafting densities. In addition, in the 13th and 15th batches, two mass-loss steps are clearly seen. The first one at 200 °C is related to non-covalently attached PFOTES molecules. (b) NMR spectra of 13th, 14th and 15th batches. Signals T2 and T3 confirm the covalently bonded PFOTES to the SiO₂ surface. These spectra also confirm that batch 14th is the one with less grafted PFOTES.

The three optimal batches, *i.e.* FG150-EA13, -EA14 and -EA15, show differences in terms of grafting density which affects the porosity of the materials and, therefore, their intrusion-extrusion performance (Figure 7b and Table 1), showing different intrusion/extrusion pressures and intrusion volume, which can be tuned depending on the operational characteristics of the prototype. All of these optimal batches show sufficient hydrophobicity and

high stability during successive intrusion–extrusion cycles. In addition, high frequency intrusion–extrusion tests were carried out by KPI partner to test the stability and performance of the material in conditions close to real-life operation.

To meet the objectives of the project and produce enough material for the intrusion–extrusion regenerative shock absorber, a process to obtain a greater quantity of this $\text{CF}_3\text{-SiO}_2$ material, hereinafter referred to as grafted silica C8- CF_3 , was initiated by using the aforementioned grafting protocol. Twelve additional batches were synthesized and, immediately after synthesis, tested in H_2O intrusion–extrusion to check if they accomplished the expected performance for the prototype. Thus, all the batches were carefully compared (Figure 12). Finally, in total, 7 grams were prepared to be used in the shock absorber prototype.

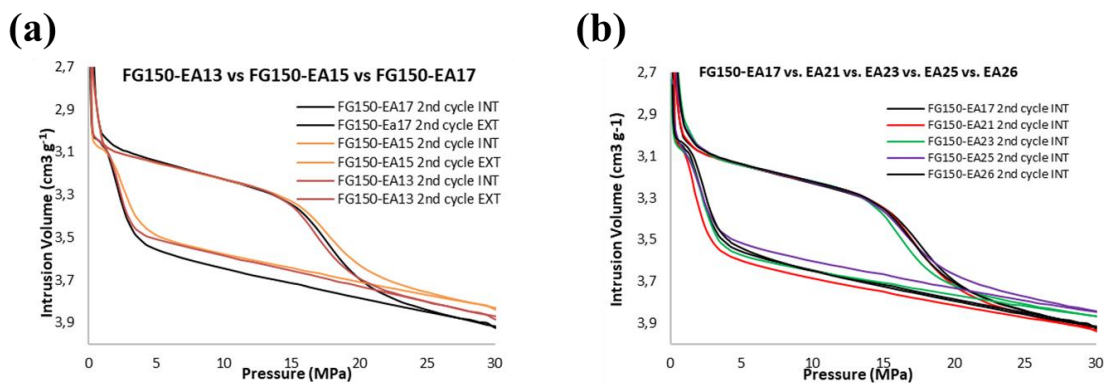


Figure 12.- H_2O intrusion–extrusion PV -isotherms of different batches of grafted silica synthesised for the shock absorber prototype (a) for 13th, 15th and 17th batches and (b) for 17th, 21st, 23rd, 25th and 26th batches.

In addition, the other four batches (1.2.2.1.13) were obtained with different grafting densities, which would be useful for further studies on the impact of different grafting densities on the H_2O intrusion–extrusion performance and, specifically, on triboelectrification.

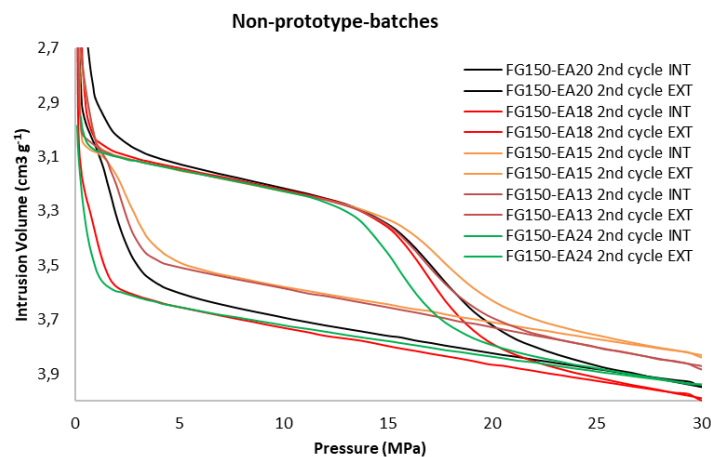


Figure 13.- H_2O intrusion–extrusion PV -isotherms of the four additional batches of grafted silica with different grafting densities to be not included in the prototype.

Also following this strategy of functionalization silicas, a mesostructured mesoporous silica (KIT 6) was chosen to be functionalized with alkyl fluorosilanes. As grafting alkyl groups, TCPFOS and TCTFPS were used and, following the literature, two different protocols of grafting were established for each grafting group. Regarding the TCTFPS, the grafting protocol began heating 0.982 g of KIT-6 under vacuum for 2 hours at 150 °C, followed by cooling under N_2 flux for

1 hour. Then, 50 ml of toluene anhydrous, 6.8 mol (0.5 ml) of pyridine and dropwise 6.8 mol (1.1 ml) of TCTFPS were added to silica letting it under stirring for 20 hours at 120 °C. After cooling, the mixture was filtered and dried overnight at 60 °C. Finally, this compound was washed with 1) toluene, 2) acetone and 3) acetone/water centrifuging each washing and then, dried for 48 hours at 70 °C. A second equivalent grafting protocol was conducted with a small number of grafting groups to avoid clogging of pores, so, for 0.495 g of KIT-6, 25 ml of toluene anhydrous, 1.5 mol (0.11 ml) of pyridine and 1.5 mol (0.25 ml) of TCTFPS were mixed. Regarding the TCPFOS, the grafting protocol of KIT-6 was quite similar to the previous one with TCTFPS, the only difference was for the washing which was performed using 1) toluene and 2) acetone. In this case, for the TCPFOS grafting, 25 ml of toluene anhydrous, 7.3 mol (0.59 ml) of pyridine and 7.3 mol (2.7 ml) of TCPFOS were added to 0.499 g of initial KIT-6. With both groups, hydrophobicity is developed in the silica KIT-6 (Figure 14).

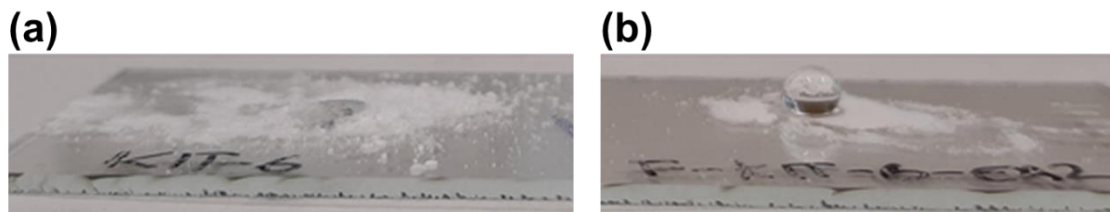


Figure 14.- (a) Pristine KIT-6 where a drop of water is infused into it and (b) functionalized KIT-6 where the developed hydrophobicity is observed.

Despite developing hydrophobicity, no intrusion/extrusion is found for both functionalizations of the KIT-6 (Figure 15). Although the presence of the fluorinated groups TCPFOS and TCTFPS was confirmed by FTIR and TGA, some issues prevent KIT-6 from being able to develop intrusion/extrusion capacity. These issues could be related to the pore clogging or the lack of grafting inside of the mesoporous of the KIT-6. In order to understand why hydrophobicity is developed but has no intrusion/extrusion capacity, ongoing analyses are carried out. Moreover, other fluorinated groups will be explored and the protocols of grafting will be improved.

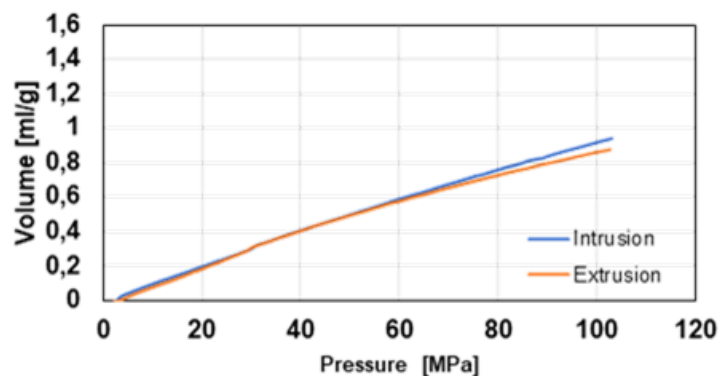


Figure 15.- PV-isotherms of a compression-decompression cycle for the KIT-6 functionalized with TCPFOS where no intrusion/extrusion is found.

2.2. CONDUCTIVE NANOPOROUS MONOLITHS

The use of conductive metals in the form of monoliths was considered as a second strategy for nanotriboelectrification. As will be shown below, such a material has a controlled current collector and allows relating the obtained results with the established contact electrification models. By this approach, the charge transfer during electrification would be enhanced as the

conductive part is chemically attached to the dielectric part where the charge is generated during the nanotriboelectrification process.

Synthesis of nanoporous conductive monoliths is challenging. For this reason, to achieve the project's tasks in time a corresponding inter-FET collaboration was established with the help of EU commission's project managers. In particular, collaboration with Ehawedry FET-Open project (www.ehawedry.eu) was organized. One of the members of Ehawedry's consortium, Prof. Patrick Huber's group, designed a doped silicon monolith with controlled nanoporosity. Next, the monolith was oxidized with H₂O₂ all over its surface creating a thin layer of SiO₂, which will be the substrate where the grafting molecule PFOTES will be attached through the same protocol described above for the first strategy with SiO₂ powders (Figure 16 and Figure 17).

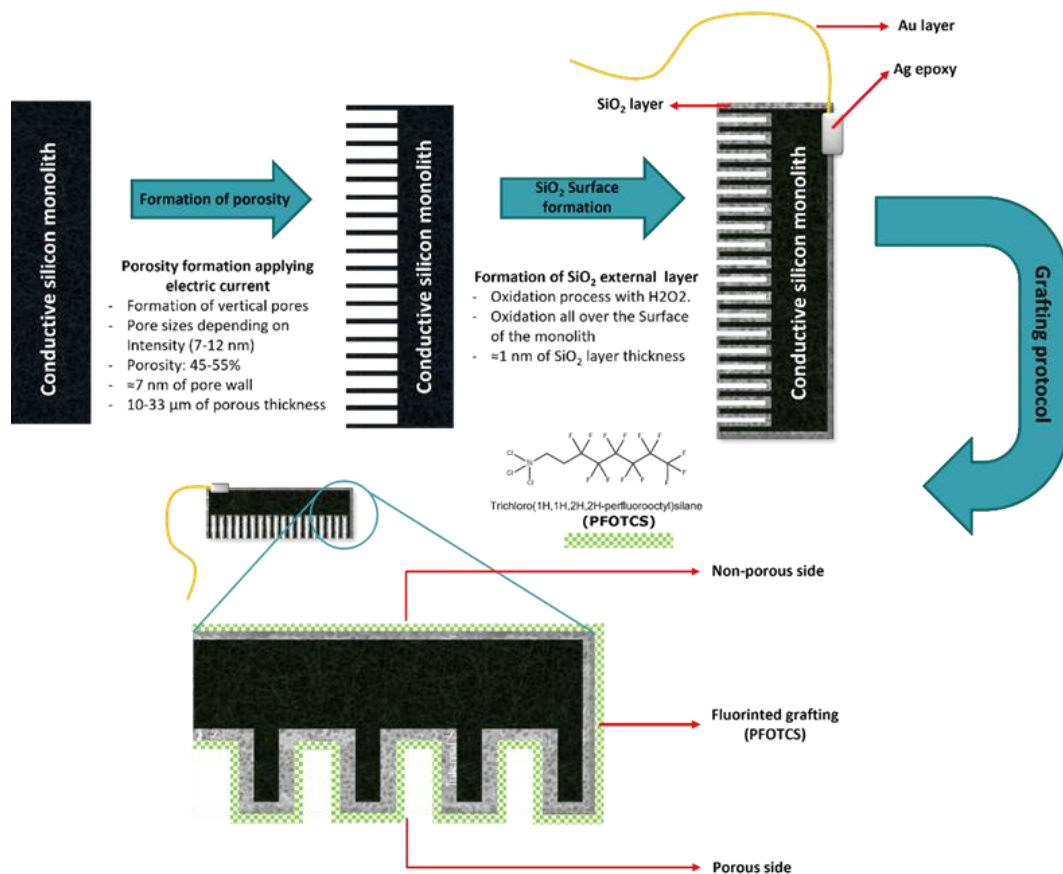


Figure 16.- Schematic process of the development of superhydrophobic Si monolith.

Three different hydrophobic monoliths were developed with different pore sizes and porous layer thicknesses:

- Monolith 0 → Pore size (\varnothing): 13.2 nm. Thickness: 33.1 μm
- Monolith I → Pore size (\varnothing): 6.2 nm. Thickness: 14.5 μm
- Monolith II → Pore size (\varnothing): 4.8 nm. Thickness: 10 μm

All of them were hydrophobized and prepared for nanotriboelectrification. As the next step in this strategy, new monoliths based on more conductive metals will be developed, to enhance the electrification process.

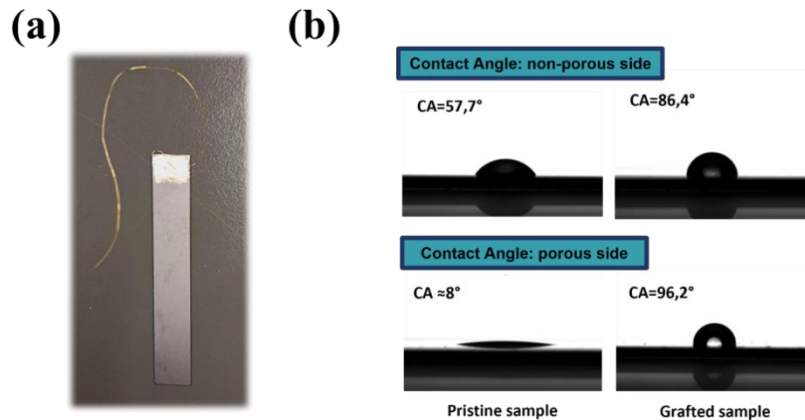


Figure 17.- (a) Monolith I before hydrophobization and (b) contact angle measurements of monolith I before and after grafting of both sides of the monolith.

2.3. HYDROPHOBIC METAL ORGANIC FRAMEWORKS (MOFs)

Finally, the last strategy involves the use of hydrophobic MOFs for nanotriboelectrification. The expected advantage from these materials is their huge surface area which can reach up to 1800 m²/g among the tested samples. With this approach, we focus on well-known microporous materials that previously demonstrated shock absorber performances such as ZIF-8, ZIF-67 and ZIF-71. Before the electrification tests, we investigated the stability issues of these three materials during H₂O intrusion-extrusion and investigated different strategies for its improvement.

In the case of ZIF-67, it is well known for its lack of stability in water⁵, which is crucial during H₂O intrusion-extrusion process. We unravelled a new feature, which enhances this behaviour, that we defined as quality. This concept lies in the synthesis protocol of ZIF-67 which could result, when is not optimal, in a non-pure material with the presence of the minor transient phase known as ZIF-L-Co⁶ the higher the concentration of this phase in the sample, the lower the quality (Figure 18).

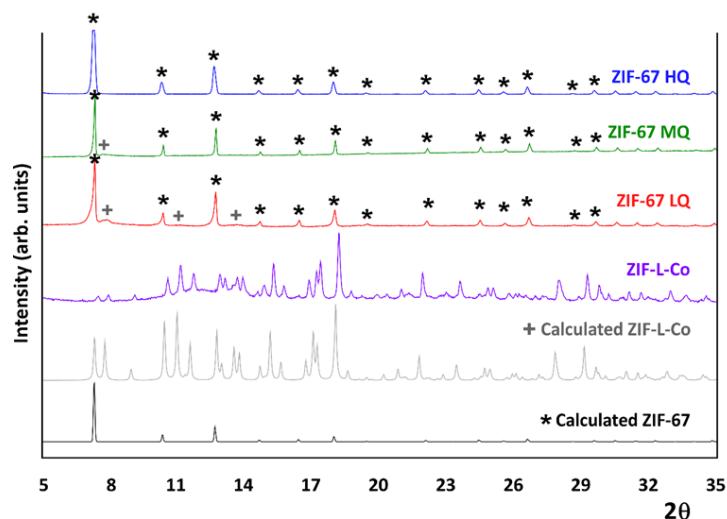


Figure 18.- XRD of different ZIF-67 qualities, ZIF-L-Co synthesized sample, theoretical model of ZIF-67 and orthorhombic ZIF-L-Co.

As expected, different quality materials exhibit different H₂O intrusion–extrusion performances. ZIF-67 HQ (high quality) with an optimal synthesis protocol, has no secondary ZIF-L-Co phase in

its structure and shows the highest V_{int} and good stability during successive intrusion–extrusion cycles. On the contrary, ZIF-67 LQ (low quality) exhibits considerably lower V_{int} and a drastic decrease in stability from the second cycle (Figure 19).

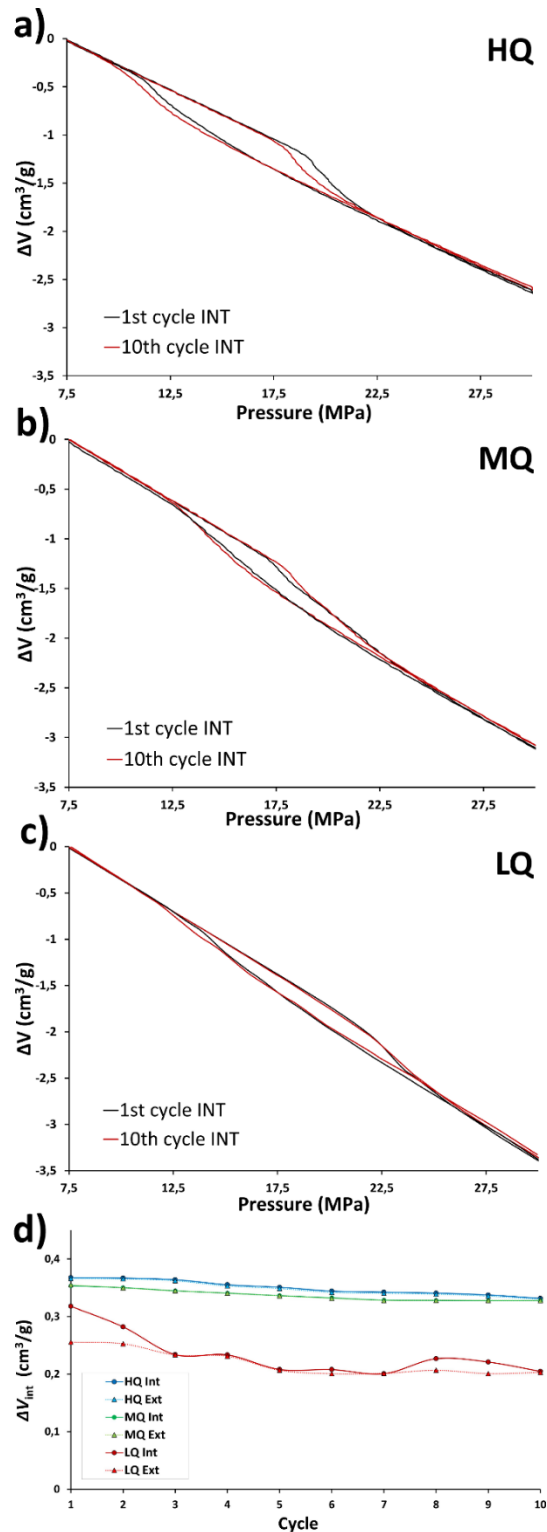


Figure 19.- PV-isotherms of (a) ZIF-67 HQ, (b) ZIF-67 MQ and (c) ZIF-67 LQ. (d) Evolution of V_{int} and V_{ext} during successive cycles of ZIF-67 HQ, ZIF-67 MQ and ZIF-67 LQ.

The same behavior was found for ZIF-8, even if it is well-known for its high-water stability compared to ZIF-67. However, it is isostructural to ZIF-67 and its synthesis protocol could result

in its homologous transient phase ZIF-L-Zn⁷. Again, the proportion of this phase in the sample results in different qualities of ZIF-8 with different V_{int} values and stability during operation cycles (Figure 20). Therefore, the understanding of the importance of the optimum protocol for higher stability during intrusion-extrusion was achieved.

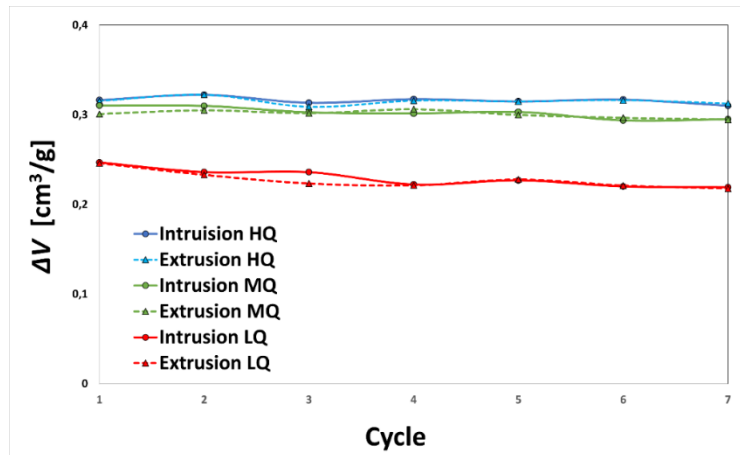


Figure 20.- Evolution of V_{int} and V_{ext} during successive cycles of ZIF-8 HQ, ZIF-8 MQ and ZIF-8 LQ.

Regarding the functionalization of MOFs, three MOFs (ZIF-67, ZIF-71 and MOF-808) were grafted. As the ZIF-67 was previously demonstrated to have intrusion–extrusion capacity with water, its grafting was intended to increase this capacity, reach liophobicity and improve stability (stability problem appears when ZIF-67 is cycled at temperatures higher than room temperature⁸). For the grafting protocol, a synthesized ZIF-67 was heated for 2 hours at 120 °C. Then 100 mg of this heated ZIF-67 were placed in a capped glass vial with 5 ml of methanol (99 %) and they were stirred until proper dispersion at 25 °C. Afterward, 50 mg of pentafluoroaniline was added letting stirring for 24 hours at 80 °C. Finally, the powder was collected by centrifugation and washed thoroughly with methanol and water. However, although the grafted ZIF-67 showed intrusion–extrusion capacity, the volume of intrusion/extrusion decreased upon cycling (Figure 21).

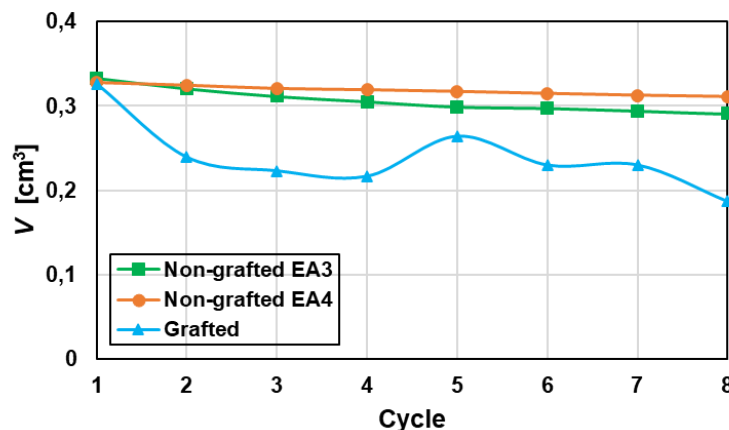


Figure 21.- Intrusion volume of non-grafted and grafted ZIF-67 depending on the compression-decompression cycle.

Although some recovery of the intrusion/extrusion capacity occurred when the grafted ZIF-67 was maintained in water at atmospheric pressure for long times, *i.e.* pauses of days between compression/decompression cycles, the capacity of intrusion/extrusion declined greatly after 12 cycles, *i.e.* around 60 days in water (Figure 22). Therefore, the stability issues for ZIF-67 were not resolved.

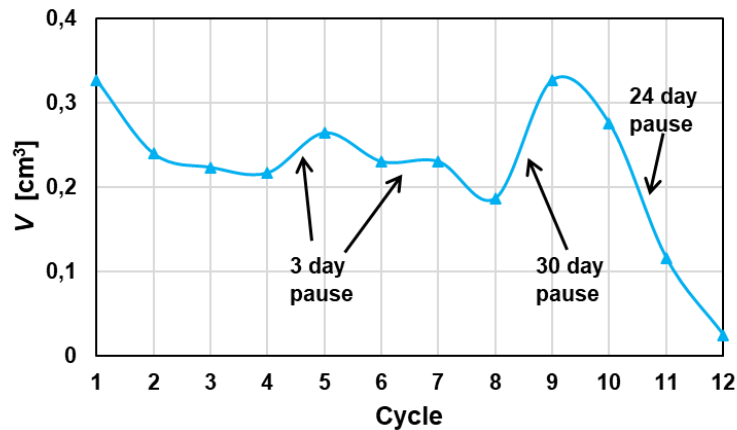


Figure 22.- Intrusion volume of the grafted ZIF-67 depending on the compression-decompression cycle with long pauses between them.

For the grafting protocol of ZIF-71, in this case, a synthesized ZIF-71 was heated for 2 hours at 120 °C. Then 100 mg of this heated ZIF-71 were placed in a capped glass vial with 5 ml of methanol (99 %) and they were stirred until a proper dispersion at 25 °C. Afterward, 60 mg of pentafluoroaniline were added letting stirring for 24 hours at 80 °C. Finally, the powder was collected by centrifugation and washed thoroughly with methanol and water. Thus, the grafted ZIF-71 showed an increment in the intrusion/extrusion capacity in water compared to the non-grafted ZIF-71 (Figure 23a). Moreover, the stability of the ZIF-71 was improved with grafting because after three compression-decompression cycles the intrusion volume decreased around 30 % for non-grafted ZIF-71 indicating degradation of this MOF, but this reduction was considerably lower for the grafted one (Figure 23b). This porous material was not considered further as it has demonstrated intrusion pressure of more than 60 MPa, which is too high for the shock absorber planned to be developed within WP4 and WP5.

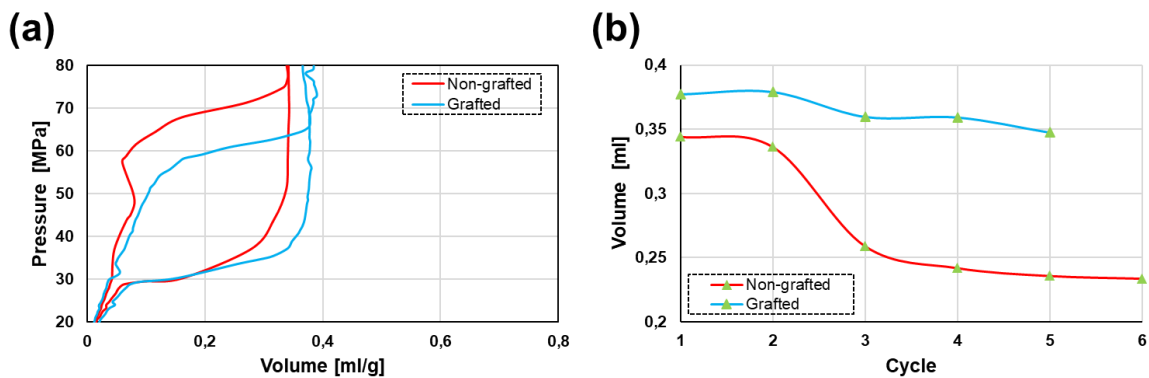


Figure 23.- Comparison for grafted and non-grafted ZIF-71 of the (a) intrusion-extrusion isotherms of the first compression-decompression cycle and the (b) intrusion volume depending on the compression-decompression cycle.

For the grafted MOF-808, the protocol followed similar steps to the previous grafted MOFs. Thus, a synthesized MOF-808 was heated for 2 hours at 120 °C. Then 100 mg of this heated MOF-808 were placed in a capped glass vial with 5 ml of methanol (99 %) and they were stirred until proper dispersion at 25 °C. Afterward, 50 mg of pentafluoroaniline was added letting stirring for 24 hours at 80 °C. Finally, the powder was collected by centrifugation and washed thoroughly with methanol and water. For this grafted MOF-808, no intrusion-extrusion performance was found upon the high-pressure compression-decompression cycle up to the pressure of 400 MPa.

The functionalization and synthesis of these and other MOFs are interesting in creating more versatile porous structures that improve their triboelectrification during intrusion–extrusion process.

Finally, we are moving this topic towards the use of hybrid MOFs, with the purpose of designing MOFs that will combine different metals or ligands that would allow to enhance properties as water stability or V_{int} or P_{int} compared to their pure metal/ligand counterparts. Additionally, tuning the intrusion/extrusion pressure is highly important for the real applications and the project's prototypes. As an example, preliminary results with hybrid ZIF composed by $\text{Co}_{0.4}\text{Zn}_{0.6}$ metallic cations randomly distributed in its SOD structure demonstrate an intermediate P_{int} compared to their pure Co-ZIF-67 and pure Zn-ZIF-8 counterparts and also an intrusion volume higher than ZIF-8. This hybrid ZIF also exhibits water stability comparable to ZIF-8 even if it contains a considerable amount of Co atoms (Figure 24). Thus, this hybrid ZIF combines the interesting properties that ZIF-8 and ZIF-67 show separately and overcomes their weaknesses, leading us to tune materials for specific heterogeneous lyophobic systems.

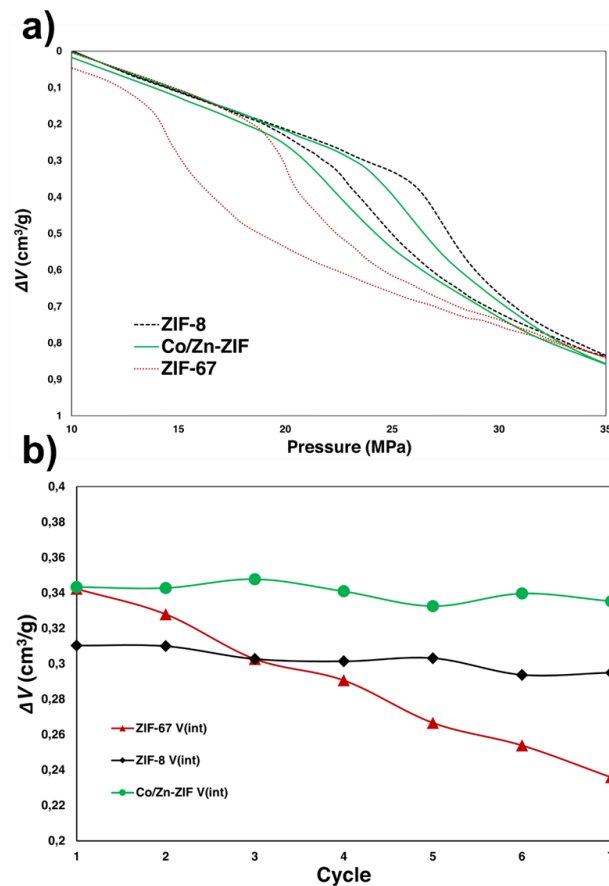


Figure 24.- (a) PV -isotherms of ZIF-8 (black dashed line), ZIF-67 (red dotted line) and Co/Zn-ZIF (green line). (b) Evolution of V_{int} during successive cycles of ZIF-67 (red line), ZIF-8 (black line) and Co/Zn-ZIF (green line).

3. NANOTRIBOELECTRIFICATION DURING INTRUSION-EXTRUSION

3.1. EXPERIMENTAL SETUP FOR NANOTRIBOELECTRIFICATION

To study the nanotriboelectrification (NTE) experimentally, a custom-made device to measure the pressure, volume and temperature (PVT) was developed. This PVT-device consists of the following main parts (Figure 25):

- a) The control and data acquisition unit: a PC and software to log the PVT-data.
- b) The high-pressure pump: a commercial unit, which achieves high-pressure via syringe-piston system.
- c) The hydraulic circuit: a series of tubes and connections to transmit the pressure into a measuring vessel where the experimental sample is placed.
- d) The electrical circuit: wires, cables and a power supply to log the electrical signal using a multimeter and an analog-to-digital converter (ADC) card connected to a laptop.

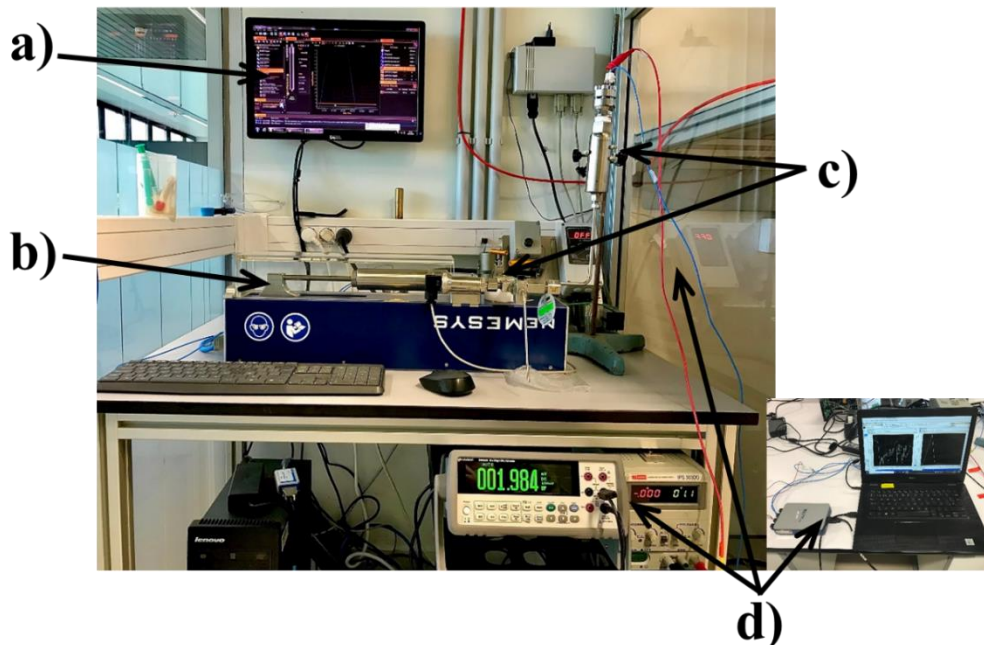


Figure 25.- Main parts of the custom-made PVT device: (a) Control and data acquisition, (b) syringe body, (c) hydraulic circuit and (d) electrical circuit.

Moreover, in order to develop and set up this PVT-device, several actions were performed as follows:

1. Assembly of the commercial CETONI syringe body and the programming of its configuration to log pressure, volume and temperature.
2. Design and construction of the vessel, where the experimental sample is placed, and its connection to the syringe body (Figure 26a).
3. Design and construction of the vessel lid with high-pressure through for electrode wires (Figure 26b).
4. Fulfilment of the safety measures and protocols to work with high pressures (Figure 26c).
5. Calibration of the PVT-device.
6. Configuration of the ADC to log the electrical signal components, *i.e.* current and voltage.

7. Synchronization of the electrical signal and pressure to ensure proper comparison of mechanical and electrical response of the system.
8. Manufacture and assembly of a heat exchanger for experiments in the range of 5 °C to 220 °C (Figure 26d).

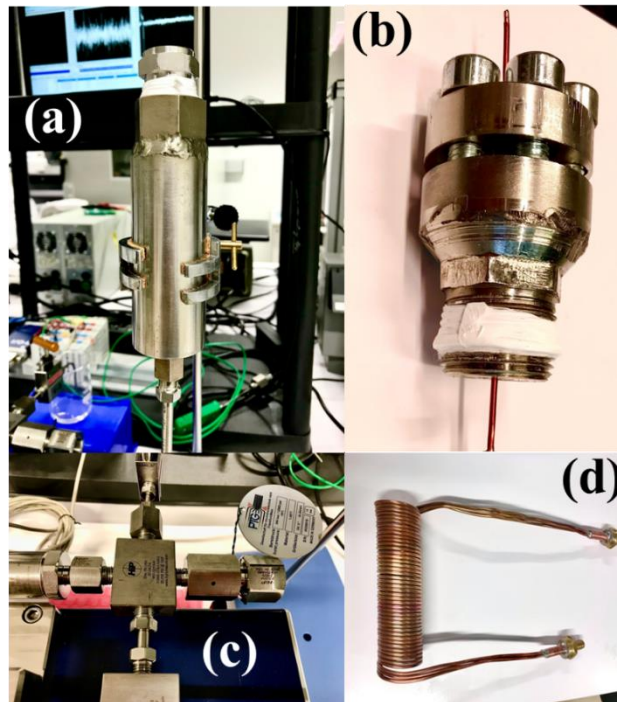


Figure 26.- (a) The vessel of PVT-device, (b) the lid to close the vessel and to pass through wires, (c) rupture disc to limit the maximum pressure in the system and (d) the heat exchanger for the vessel.

3.2. NANOTRIBOELECTRIFICATION EXPERIMENTAL STUDY DURING INTRUSION-EXTRUSION

Once the experimental custom-made setup was ready and demonstrated to be fully satisfactory for the project's tasks execution, the experimental work to understand the nanotriboelectrification of nanoporous materials and NWLs was carried out. Three electrical configurations, *i.e.*, active powder configuration, passive powder configuration and passive monolith configuration (Figure 27) were tested.

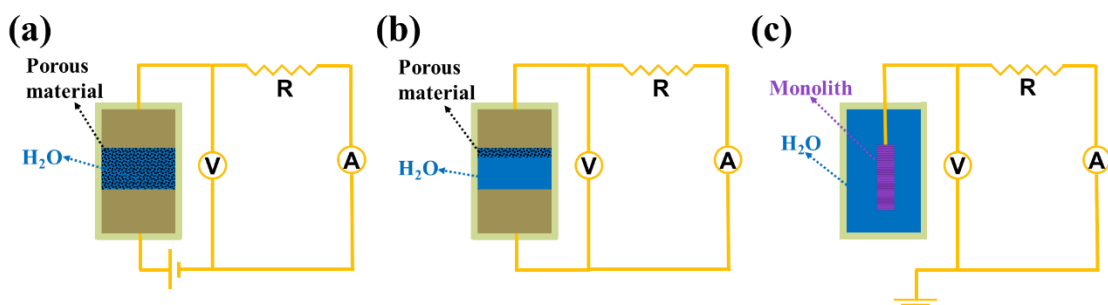


Figure 27.- Schematic circuits for (a) active configuration, (b) passive configuration and (c) monolith configuration.

For the double-electrode active (Figure 27a) and passive (Figure 27b) configurations, a 3D-printed cell was used to keep the distance between the electrodes (Figure 28a). Stainless steel electrodes were used to avoid any electrochemical issues during electrification. For passive configuration, one electrode was the counter electrode and it was located into the measuring

vessel, another electrode was in direct contact with the porous material (Figure 27b). For the monolith configuration, the silicon monolith (see details in Section 2.2 and Figure 16) was connected to the circuit directly using a thin gold wire pasted with a silver conductive paint to the non-porous side of the conductive silicon monolith (Figure 28b).

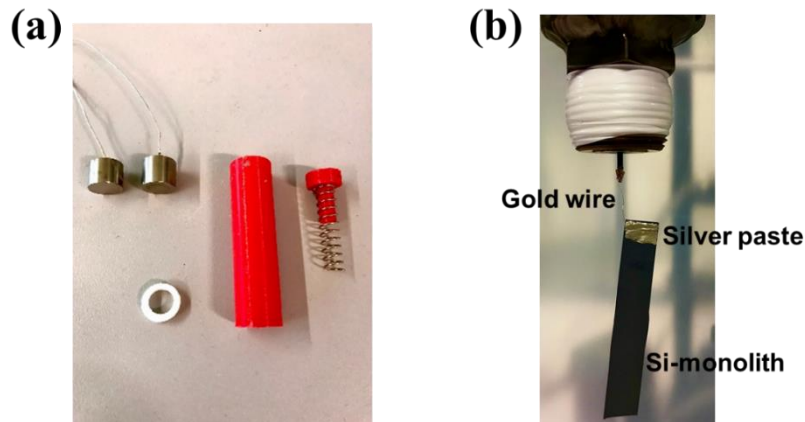


Figure 28.- Schematic circuit for the double-electrode passive configuration where the porous material is only touching one electrode.

3.2.1. ACTIVE CONFIGURATION

The first strategy to measure NTE implied a double-electrode configuration with an active circuit (Figure 27a), *i.e.* a circuit where a bias voltage is applied by a power supply.

In this configuration, the grafted silica C8-CH₃ was used as porous material and distilled water as NWL. The grafted silica was located between the two electrodes, which were separated by 5.2 mm and were both in contact with the PM. To maintain the distance between the electrodes during testing, PTFE spacers were used. All (electrodes, spacers and silica C8-CH₃) were put into a 3D-printed cell which was connected to the external electrical circuit through the lid. Finally, the cell was covered by silicone to electrically insulate the electrodes, grafted silica and NWL from the pressure-transmitting fluid and the cell (Figure 29). Silicon encapsulation was used as it provides both insulation as well as flexibility, which requires the transmission of pressure. Then, compression–decompression (intrusion–extrusion) tests were carried out at pressures of up to 300 bar, applying different bias voltages.

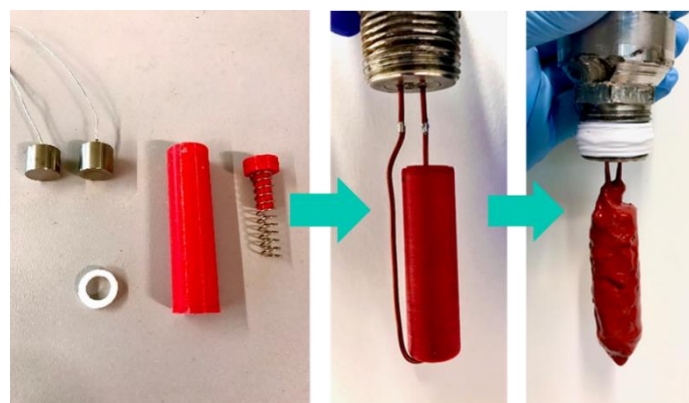


Figure 29.- 3D-printed cell, electrodes and spacers to be connected electrically and insulated by silicone for the double-electrode active configuration.

The analysis of the results shows that the electrification is observed exactly when the intrusion/extrusion of water into/from nanopores occurs (Figure 30).

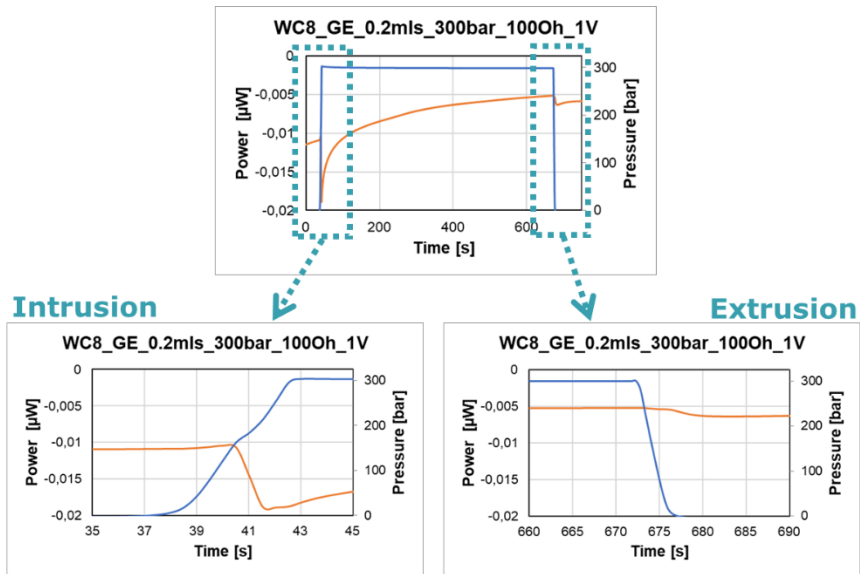


Figure 30.- Electrical signal (orange line) and pressure (blue line) of a compression–decompression test at 0.2 ml/s for the double-electrode active configuration.

Then, the energy generated during intrusion–extrusion can be calculated by integrating the area of the peaks obtained for the electrical power over time (Figure 31).

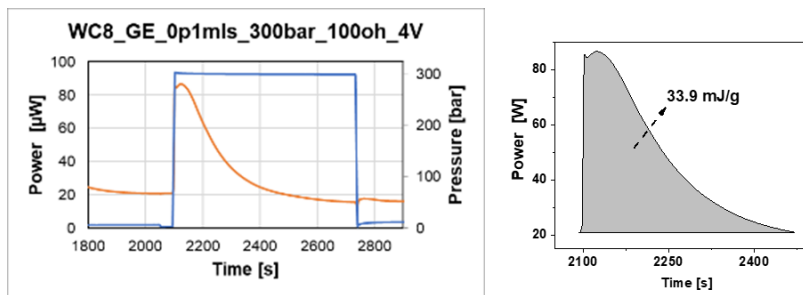


Figure 31.- Electrical power (orange line) of a compression/decompression test at 0.2 ml/s for the double-electrode active configuration and the corresponding generated energy calculated by integration.

From the results of the tests with different bias voltages, it is found that the electrical output generated strongly increases with the applied bias voltage (Figure 32).

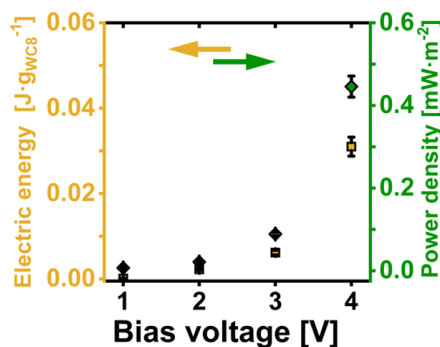


Figure 32.- Effect of the applied bias voltage on the generated electrical energy and power density for the double-electrode active configuration using a distance between the electrodes of 5.2 mm. $R=100\ \Omega$.

In order to study if the distance between electrodes affects the generation of electrical energy in the double-electrode configuration with an active circuit (Figure 27a), this distance was reduced to 1.77 mm from 5.1 mm. The cell where the porous materials are placed was the same as in previous experimental tests, but some spacers were removed from between the

electrodes. A similar protocol to previous tests was followed to insulate the cell and connect it to the circuit (see Figure 29). Also, as previously, compression–decompression tests were carried out at pressures up to 300 bar whilst applying different bias voltages. Overall, more than 50 intrusion-extrusion cycles were performed.

The results with different bias voltages show analogous behaviour to the previous results using a longer distance between electrodes, *i.e.* the generated electrical energy increases with the applied bias voltage (Figure 33). However, the effect seems to be more pronounced when the distance is shortened between electrodes. This fact suggests that an effective electric field has a strong effect on the generated electrical energy during the intrusion-extrusion cycle.

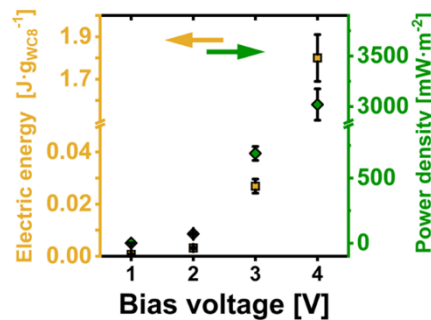


Figure 33.- Effect of the applied bias voltage in the generated electrical energy and power density for the double-electrode active configuration using a distance between electrodes of 1.77 mm. $R=100\ \Omega$

From these results, the factor of efficiency upon an intrusion–extrusion cycle can be estimated for this double-electrode active configuration. This factor of efficiency is calculated by dividing the generated electrical energy E_{elc} and the work done W_{mec} during the intrusion–extrusion cycle. For the heterogeneous lyophobic systems of grafted silica C8-CH₃ and water, the supplied work to the system during intrusion W_i was $8.5\ \text{J}\cdot\text{g}^{-1}$ and, during extrusion, the released work W_e was $1.3\ \text{J}\cdot\text{g}^{-1}$. The efficiency of this configuration is as follows:

$$\frac{E_{elc}}{\Delta W_{mec}} = \frac{E_{elc}}{W_i - W_e} = \frac{1.8}{8.5 - 1.3} = 0.25$$

Therefore, the electrical energy obtained corresponds to approx. 25 % of the mechanical work done during the intrusion–extrusion cycle for this double-electrode active configuration using a distance between electrodes of 1.77 mm when a bias voltage of 4 V is applied. It is important to highlight that this conversion efficiency is provided here just as the first experimental evidence to give an idea of the order of magnitude. The system is not yet optimized for maximum energy generation (electrode distance and configuration, porous material and NWL, bias voltage and resistance, *etc.*).

This double-electrode active configuration revealed two main drawbacks that for the moment prevent it from being an efficient layout to generate electrical energy via Electro-intrusion principles:

- The slow kinetics discharge after intrusion/extrusion, where hundreds of seconds are needed to recover the base electrical signal (see Figure 31). For the target application in this project, *i.e.* car shock absorber, this is too slow.
- Material degradation under applied voltage. The grafted silica C8-CH₃ during these experiments degraded, reducing the volume of intrusion/extrusion when the material was subjected to 4 V for almost 12 h (Figure 34).

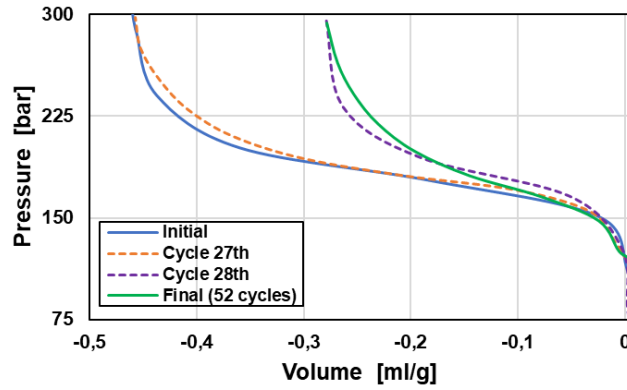


Figure 34.- Intrusion isotherms of grafted silica C8-CH₃ for the double-electrode active configuration. It can be noted between cycle 27 and cycle 28 the intrusion volume decreases due to the system being, between these two cycles, under 4 V for almost 12 h.

Considering the previous results, degradation of porous material was thought to be the reason for reduced electrification. Therefore, after experiments with bias voltage, the same material was subjected to intrusion–extrusion cycles with zero bias voltage (Figure 27a) to check the electrification behaviour again. It was found that the amplitude of the peaks was greatly reduced (Figure 35). Therefore, the grafted silica C8-CH₃ seemed to degrade and its electrification capacity was reduced.

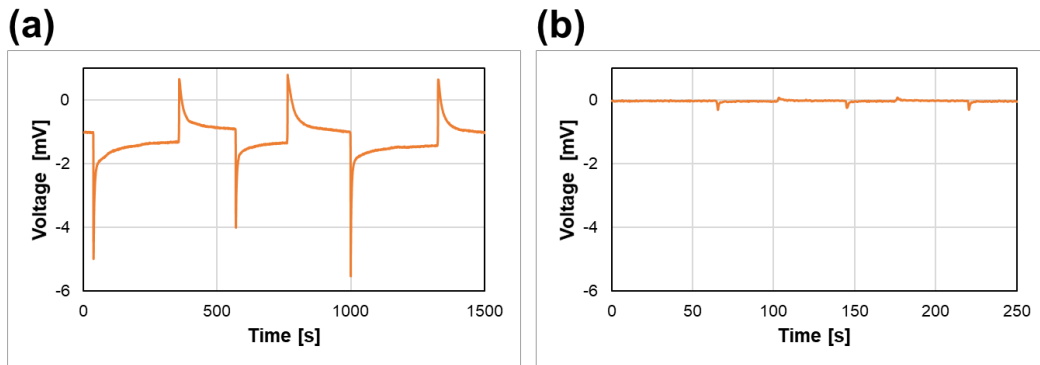


Figure 35.- Voltage signal for three compression/decompression cycles (a) before and (b) after applying bias voltages for the double-electrode passive configuration.

Finally, two effects during electrification were noted when comparing with passive configuration (see Section 3.2.2). Firstly, the kinetics of the signal was slowed compared with the double-electrode passive configuration. Secondly, the direction of the intrusion and extrusion peaks were not opposed, *i.e.* both peaks were in the same direction (Figure 36).

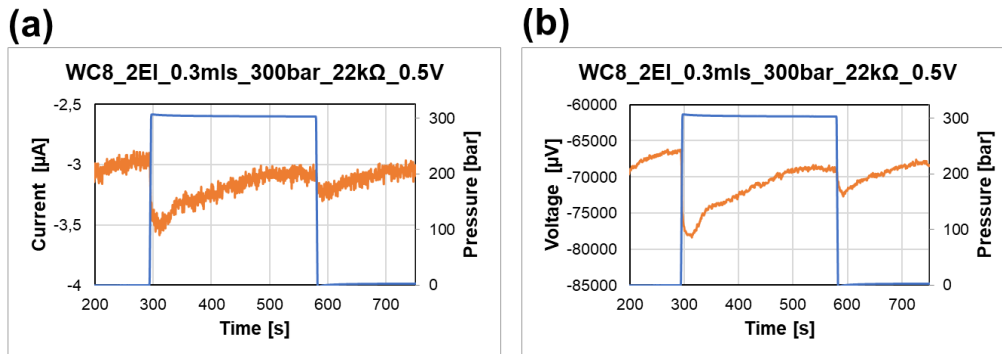


Figure 36.- (a) Current and (b) voltage during a compression/decompression cycle for the double-electrode active configuration with an applied bias voltage of 0.5 V.

3.2.2. PASSIVE CONFIGURATION

To avoid porous material stability, the passive configuration was considered (Figure 27b). Without bias voltage, asymmetry must be introduced between the two electrodes to observe any potential difference upon water intrusion electrification. Therefore, the porous material was brought in direct contact and constrained to only one of the electrodes in the passive configuration (Figure 27b). This provides a potential difference between the electrodes upon intrusion–extrusion-provoked electrification. Several important findings were identified during this experimental campaign. 1) the contact of PM with the electrode seems to play an important role in charge collection during the intrusion-extrusion process. 2) Using the ground as a counter electrode provides unwanted fluctuations to the baseline of the electrical signal. Considering these results, it was suggested to introduce the counter electrode into the measuring vessel.

For this double-electrode passive configuration, a 3D-printed cell was used to keep the distance (10.75 mm) between the electrodes (Figure 28a). Stainless steel electrodes were used to avoid any electrochemical issues during electrification. The mass of grafted silica C8-CH₃ was 0.05 g. Finally, the cell was covered by silicone to insulate it. Then compression/decompression tests were carried out up to 300 bar.

It was found that noticeable electrification occurred upon intrusion–extrusion process. However, contrary to the active scheme the sign of the current is different for intrusion and extrusion (Figure 37). Furthermore, the kinetics of discharge had improved by around two orders of magnitude from almost hundreds of seconds for the double-electrode active configuration to seconds for the passive one (Figure 37). This configuration also revealed no degradation of porous material.

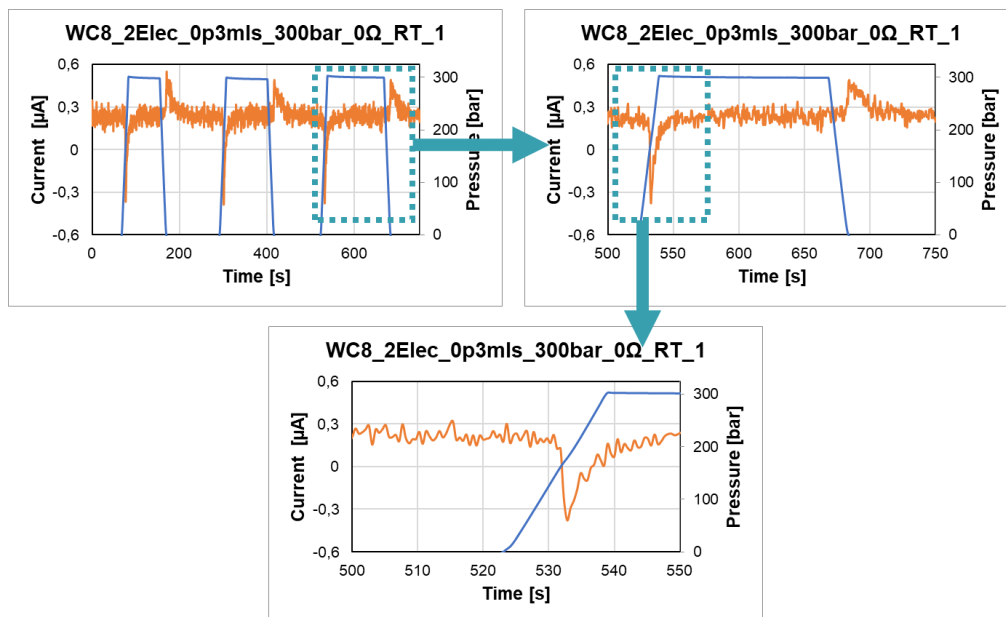


Figure 37.- Results of three compression-decompression cycles for the double-electrode passive configuration, along with magnifications of a single cycle and its corresponding intrusion.

Considering that the two main issues of the active configuration (degradation and slow kinetics) were resolved for the passive scheme, a systematic study of the main parameters affecting the electrification was initiated. The goal of such studies is 1) to understand the mechanism behind the intrusion-extrusion electrification and 2) to maximize the electrical output in the intrusion-extrusion cycle. In particular, to analyse the obtained results for this double-electrode

passive configuration, two parameters were established: the maximum current (Figure 38a), *i.e.* the peak of the current signal when the intrusion/extrusion occurs, and the energy integrating the electrical power over time (Figure 38b).

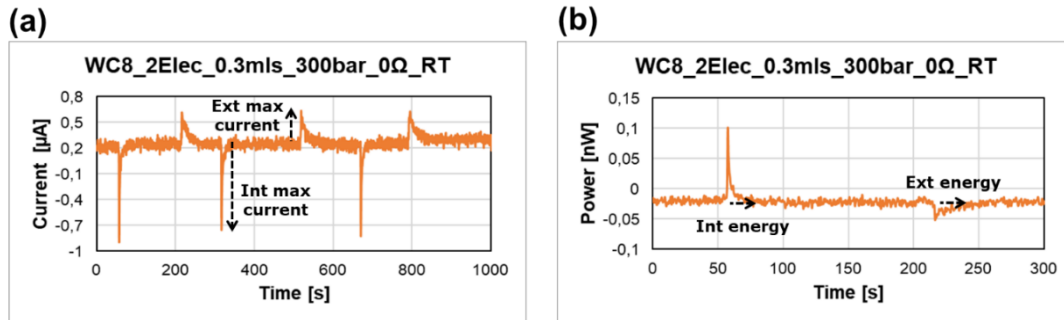


Figure 38.- Parameters to study electrification for the double-electrode passive configuration: **(a)** maximum current and **(b)** energy.

Firstly, the effect of the compression/decompression rate was studied. Regarding the maximum current, there was a clear increase in the current peak with the increase in the compression/decompression rate (Figure 39). Moreover, an asymmetry between intrusion and extrusion maximum currents was found, *i.e.* the intrusion peaks are larger than extrusion peaks for the current. This could be related to different kinetics of the intrusion/extrusion process, which is known from previous studies. It can be seen that maximum current increases with compression-decompression rate up to around $0.2 \text{ ml}\cdot\text{s}^{-1}$. So higher rates do not provide a noticeable increase in the maximum generated current.

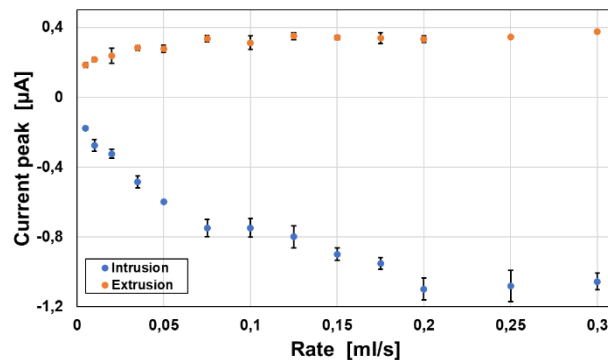


Figure 39.- Maximum current at intrusion and extrusion depending on the compression/decompression rate.

However, the generated energy appears to be independent of the compression/decompression rate as there is no clear trend from the obtained results (Figure 40). These dependencies suggest that within the range of tested rates, the mechanism of electrification does not change.

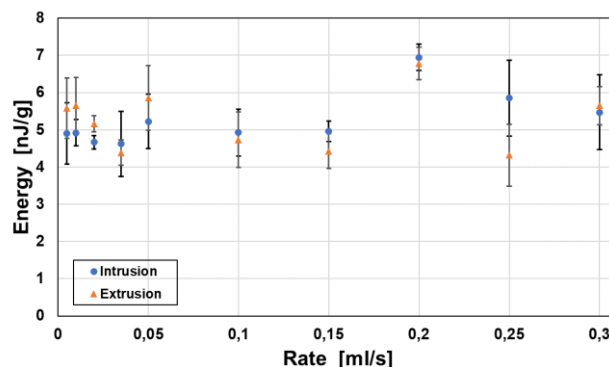


Figure 40.- Generated energy at intrusion and extrusion depending on the compression/decompression rate.

Secondly, the effect of the temperature was considered. Therefore, the heat exchanger (Figure 26d) was used to hold the system at 5.5 °C (Figure 41) for the same double electrode passive configuration where grafted silica C8-CH₃ is only touching one of the electrodes (Bartolomé et al. Triboelectrification during water intrusion–extrusion into-from hydrophobic nanopores. Submitted 2024.).

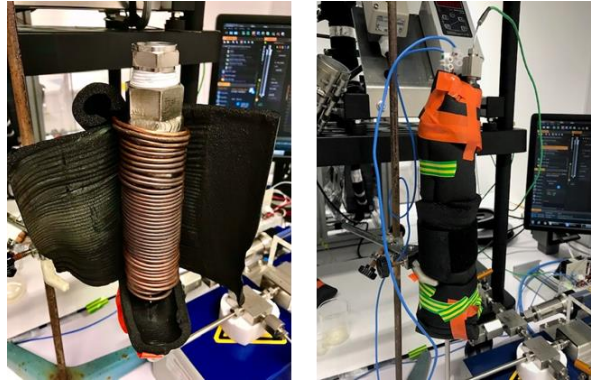


Figure 41.- Vessel of PVT-device with the heat exchanger and the thermal insulation to carry out experimental tests at 5.5 °C.

As it can be seen in Figure 65, the generated current increases with temperature. The dependence on compression rate was found to be qualitatively similar for both temperatures.

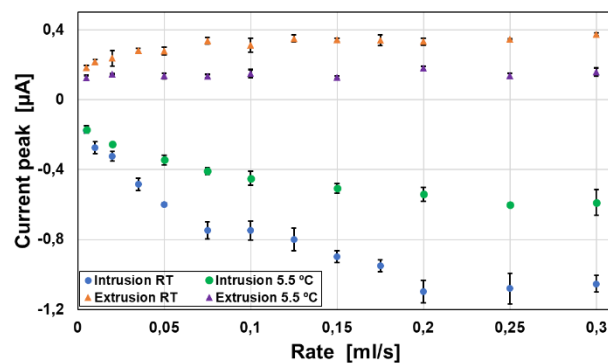


Figure 42.- Maximum current at intrusion and extrusion into and from C8-CH₃ depending on the compression/decompression rate comparing room temperature and 5.5 °C.

Similarly, for room temperature experiment, electrical energy was found to be independent of the compression-decompression rate at 5.5 °C (Figure 43). On the other hand, the energy slightly decreases with temperature for both intrusion and extrusion, though this decrease is more evident for the extrusion (Figure 43).

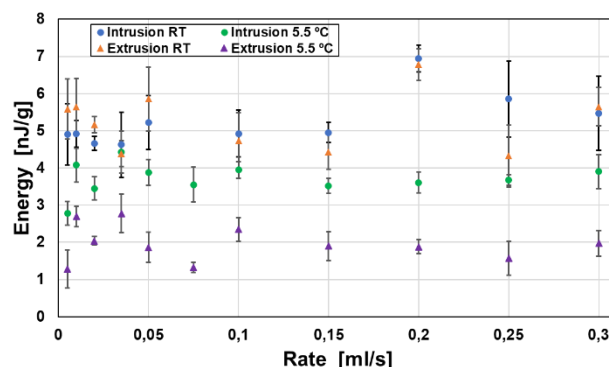


Figure 43.- Generated electrical energy during intrusion and extrusion of water into and from C8-CH₃ depending on the compression/decompression rate at room temperature and 5.5 °C.

Resistance in the circuit is an important parameter affecting the energy output. In all previous experiments with the double-electrode passive configuration (Figure 27b), a resistor of $0\ \Omega$ was used. This was done to maximize the generated current for the analysis provided above. Therefore, to find the optimal value, the resistor of the circuit was varied in the performed compression/decompression tests up to 300 bar with the rate of $0.3\ \text{ml}\cdot\text{s}^{-1}$. In this experiment, both voltage and current were measured to calculate the electrical output power (Figure 44).

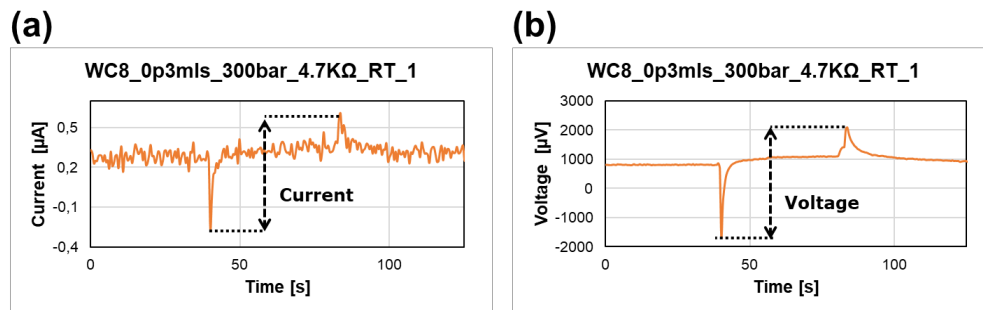


Figure 44.- Parameters to optimize the electrical resistance for the double-electrode passive configuration: (a) current and (b) voltage amplitudes.

Using the results for the current and voltage amplitudes at different electrical resistances (Figure 45a), it was found that the maximum power density for this double-electrode passive configuration was between 10-30 kΩ (Figure 45b).

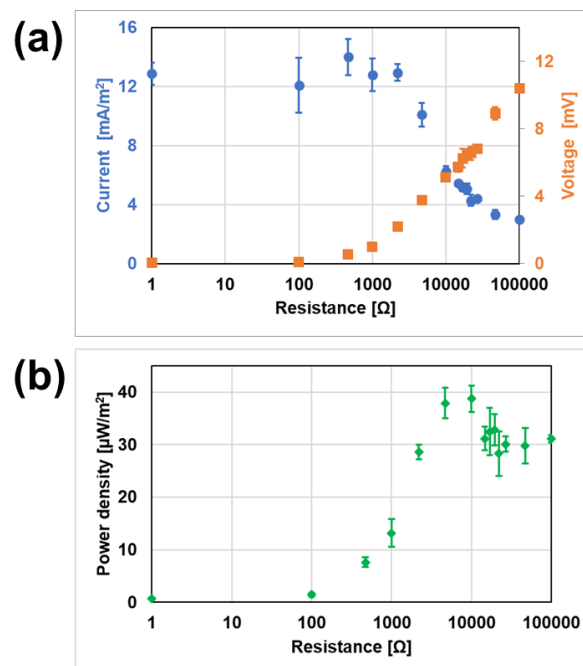


Figure 45.- (a) Current and voltage amplitudes and (b) power density at different electrical resistances in the circuit of the double-electrode passive configuration with the system $\{\text{H}_2\text{O} + \text{C}_8\text{-CH}_3\}$.

Once the optimal electrical resistance was determined, the effect of cycling in the electrification was studied. Thus, the compression–decompression tests up to 300 bar at $0.3\ \text{ml}\cdot\text{s}^{-1}$ were carried out with severely reduced waiting times at maximum and minimum pressures, *i.e.* almost non-stop compression/decompression cycles were carried out (Figure 46a). The dwell times used were 1 ms, 1 s and 2 s. From the power density results at different waiting times, a steady state was found after the third compression/decompression cycle (Figure 46b). Moreover, the steady power density value was around half of the power density in the first cycle. The results were found to be independent of the dwell time (Figure 46b).

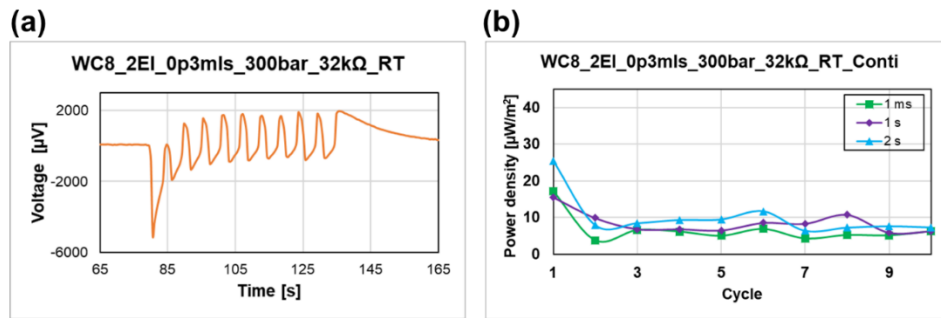


Figure 46.- (a) Voltage signal for 10 compression–decompression cycles with a waiting time of 1 s and (b) power density depending on the compression–decompression cycle at different waiting times.

The passive configuration was also used to investigate the nanotriboelectrification behaviour of different porous materials, *e.g.* the MOF ZIF-8 and the fluorinated grated silica C8-CF₃.

As previously, the mass of ZIF-8 was 0.05 g and the cell (Figure 29) was covered by silicone to insulate it. The compression and decompression rates are 0.3 ml·s⁻¹. For ZIF-8, a clear difference is found compared with grafted silica C8-CH₃, for both intrusion and extrusion, the peaks are in the same direction (Figure 47). This result is surprising and may suggest material degradation.

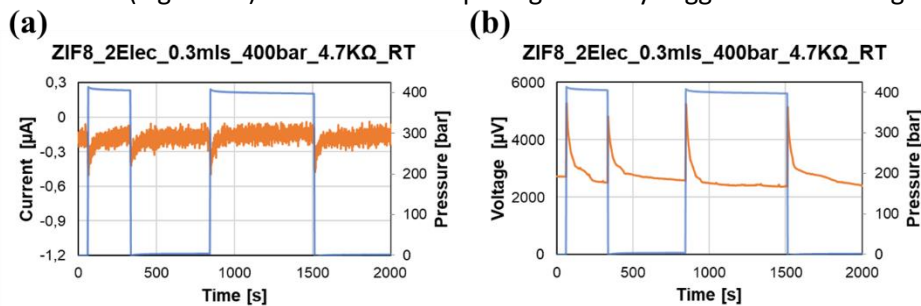


Figure 47.- (a) Current and (b) voltage during a compression–decompression cycle for the double-electrode passive configuration with MOF ZIF-8.

From the results for the current and voltage amplitudes at different electrical resistances with ZIF-8 (Figure 48a), the optimal resistor is found that it is around 10 kΩ obtaining the maximum power density (Figure 48b). This optimal resistance for ZIF-8 is similar to the one obtained for the grafted silica C8-CH₃.

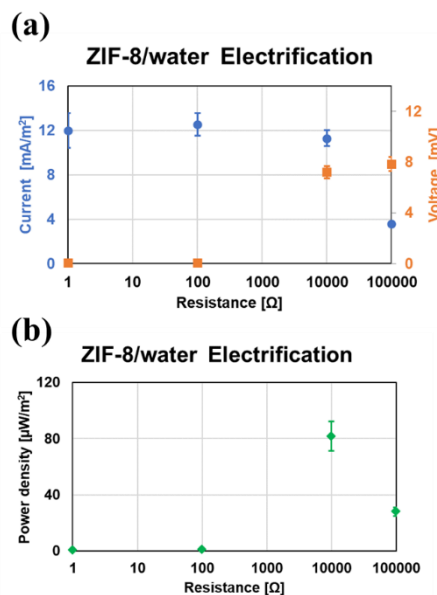


Figure 48.- (a) Current and voltage amplitudes and (b) power density at different electrical resistances in the circuit of the double-electrode passive configuration with MOF ZIF-8.

When the generated energy per cycle is compared between the ZIF-8 (Figure 49a) and the silica grafted silica C8-CH₃ (Figure 49b), it was found an increment of around one order of magnitude.

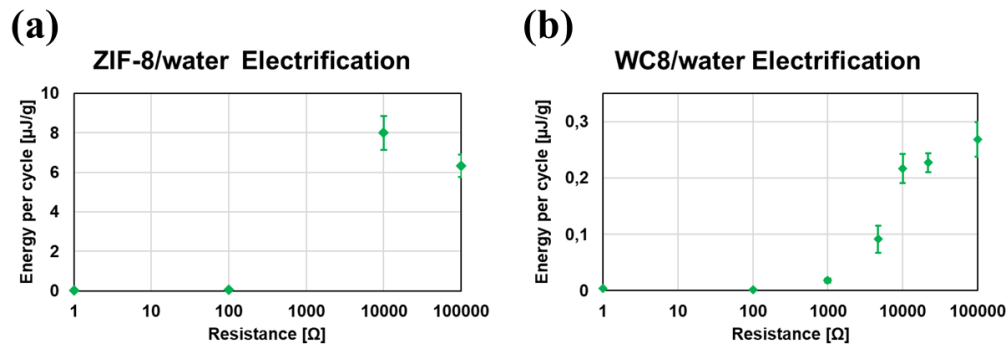


Figure 49.- Generated electrical energy per cycle during intrusion-extrusion of water into-from (a) MOF ZIF-8 and (b) grafted C8-CH₃ silica for the double-electrode passive configuration.

Using also this double-electrode passive configuration with MOF ZIF-8, the intrusion liquid was changed to heavy water D₂O. Moreover, a water solution of fullerene C₆₀ was also tested as intrusion liquid to increase the liquid conductivity. Although these liquids increase the energy per cycle (Figure 50), the dispersion also increases, finding a gradual decay with cycles. Therefore, the use of other liquid than water for electrification tests becomes promising but more complicated chemical interactions should be considered to explain the gradual decay in energy generation with cycles.

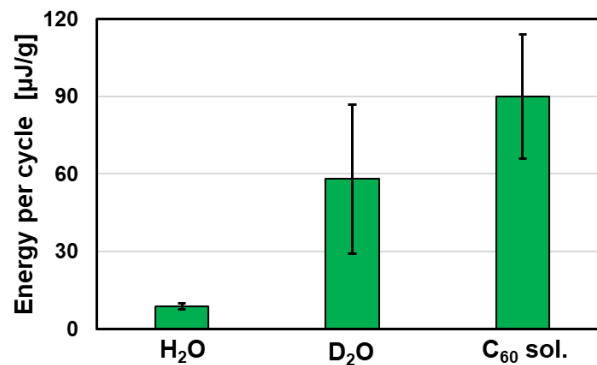


Figure 50.- Generated electrical energy per cycle during intrusion-extrusion of different liquids into-from MOF ZIF-8 for the double-electrode passive configuration.

Moreover, the crystallite size of MOF ZIF-8 was investigated using a nanoZIF-8 which has a crystallite size of 10-12 nm in comparison with 86-87 nm of the regular ZIF-8. The clear effect of using a smaller crystallite size is the reduction of the intrusion/extrusion pressures as well as the intrusion volume (Figure 51). Thus, the energy generated by the nanoZIF-8 is also decreased to 5.2 μJ/g from the 9 μJ/g of the ZIF-8.

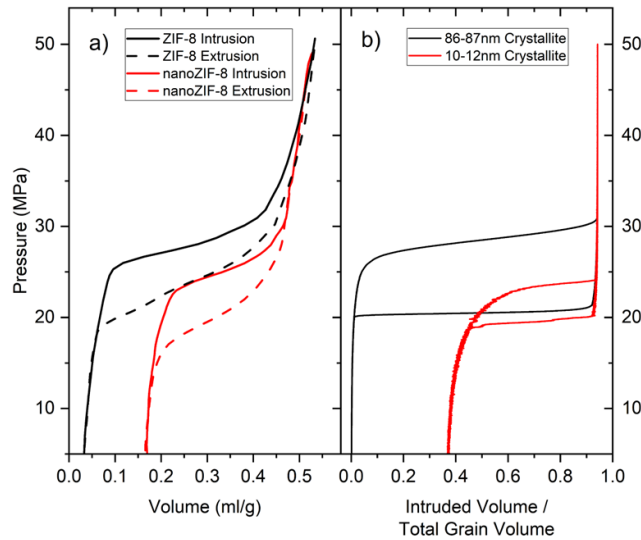


Figure 51.- Generated electrical energy per cycle during intrusion-extrusion of different liquids into-from MOF ZIF-8 for the double-electrode passive configuration.

Finally, the grafted silica with fluorinated groups, *i.e.* C8-CF₃ (see Section 2.1) was tested using a double-electrode passive configuration (Figure 27). This fluorinated silica was tested in two different forms, *i.e.* as powder and as a pellet. The powder as the previous test with silica C8-CH₃ and the pellet to gain charge transfer between porous material and electrode. Both the powder and the pellet with the same mass of 0.05 g and the same compression/decompression rate of 0.3 ml·s⁻¹.

After analysing the results of the voltage and current peak amplitudes in comparison with powder ZIF-8 and silica grafted silica C8-CH₃ (see Table 2), we find that the performance of the grafted silica C8-CF₃ is better in both pellet and powder than the silica C8-CH₃ despite the lower porosity, 0.53 cm³/g for silica C8-CH₃ and 0.41 cm³/g for silica C8-CF₃. Comparing with the power ZIF-8, both materials in powder show similar electric behaviour. The pellet of grafted silica C8-CF₃ doubled the electrical performance, probing that the pellet presentation increases the surface contact between porous material and electrode, *i.e.* the charge transfer is improved.

Table 2.- Peaks amplitudes for different materials using 22 KΩ.

	C8-CF₃ (pellet)	C8-CF₃ (powder)	C8-CH₃ (powder)	ZIF-8 (powder)
ΔV [mV]	28±1	13.2±0.6	6.5±0.4	13.4±0.4
ΔA [μA]	1.37±0.07	0.71±0.05	0.34±0.03	0.68±0.04
ΔP [nW]	38±4	9.4±0.9	2.2±0.3	9.1±0.7

As the grafted silica C8-CF₃ exhibits a better electrical performance than silica C8-CH₃ and the silicas show good stability in water, the silica C8-CF₃ was chosen as the porous material to be used in the prototype developed by the consortium. Therefore, some cycling tests were carried out with this silica to see the electrical performance. Thus, ~150 cycles were carried out with a frequency of 0.075 Hz. The results show a reduction in the first cycles to a steady value for the rest (Figure 52). The material shows no sign of degradation after this cycling.

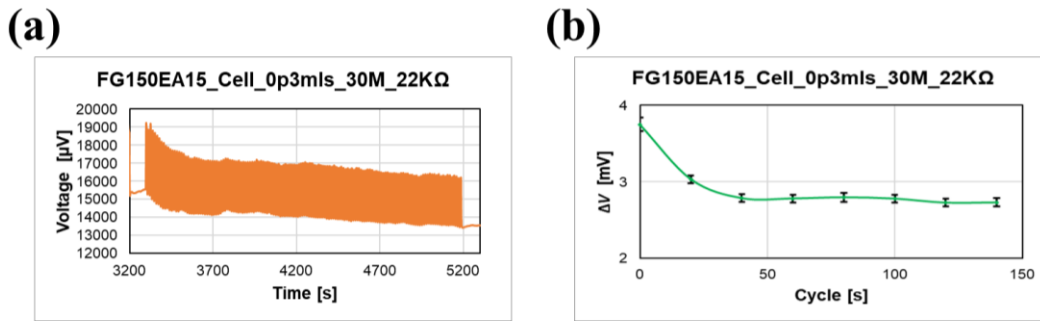


Figure 52.- (a) Voltage signal during 147 cycles at 0.075 Hz. (b) Voltage peak amplitude progression with the cycles, an average of 20 cycles.

Figure 53 shows how the generated energy per cycle has progressed during the project time for the double-electrode passive configuration. It can be found an increment of almost three orders of magnitude from the initial nanotriboelectrification tests. Although this passive configuration will continue being tested, other configurations as the monolith configuration where a porous conductive electrode is introduced to improve the charge transfer created during the intrusion-extrusion will be prioritised.

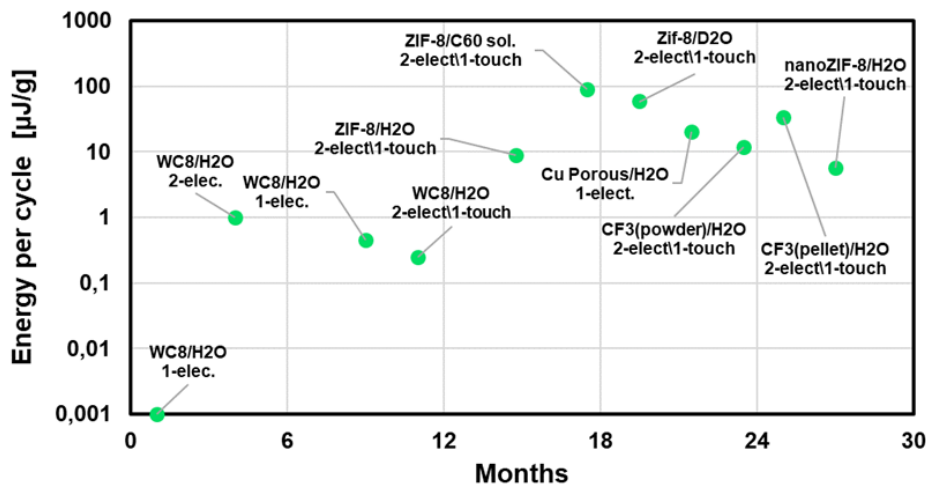


Figure 53.- Progression of the generated energy per intrusion-extrusion cycle for different materials and configurations.

3.2.3. MONOLITH CONFIGURATION

As we pointed out above, the monolith configuration (Figure 27c) was used to increase the charge transfer of the system due to the silicon monolith (electrode) itself experiencing intrusion-extrusion on the surface pores. Three samples (named 0, I and II) with different pore sizes and porous layer thicknesses (see Figure 54) were tested to investigate the nanotriboelectrification.

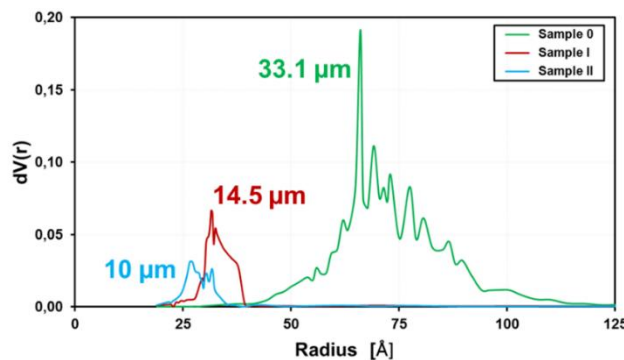


Figure 54.- Pore size and porous layer thickness of the three samples of Si-monolith.

Firstly, the circuit connections of the monolith configuration (Figure 55) were studied. On the one hand, the connection of the positive or negative terminal of the ammeter was studied to see if the ammeter polarity affects the intrusion-extrusion generated energy. And by the other hand, the connection of the circuit to the ground or to a counter electrode as the metallic vessel.

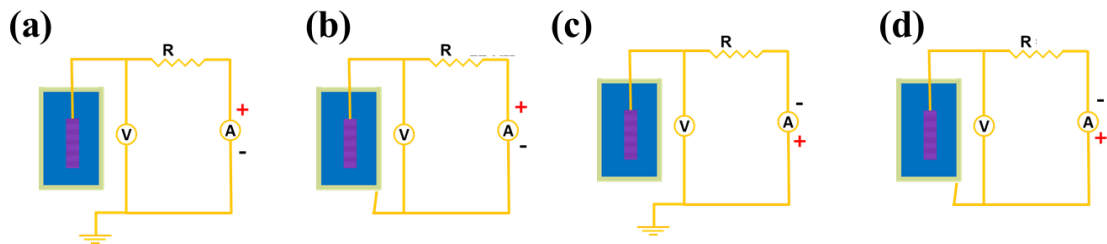


Figure 55.- Circuit connections for the monolith configuration: **(a)** monolith connected to positive terminal del ammeter and then ground, **(b)** monolith connected to positive terminal del ammeter and then metallic vessel, **(c)** monolith connected to negative terminal del ammeter and then ground and **(d)** monolith connected to negative terminal del ammeter and then metallic vessel.

The results show that the connection directly to the ground generates more electrical energy and especially when the monolith sample is connected to the positive terminal of the ammeter (Figure 56). Therefore, this connection (Figure 55a), *i.e.* monolith sample to the positive terminal of the ammeter and then ground, was used as a circuit connection to investigate the nanotriboelectrification of Si-monolith samples.

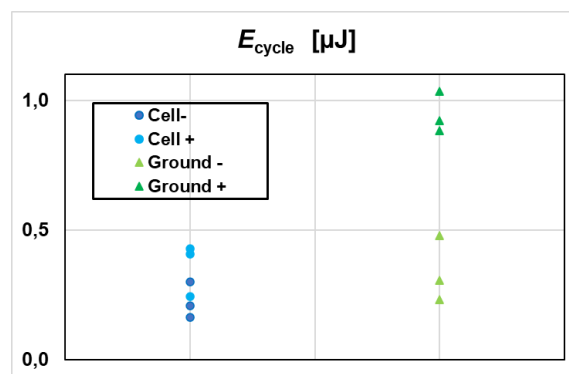


Figure 56.- Generated energy per intrusion-extrusion cycle for different circuit connections for the monolith configuration with sample II.

As the Si-monolith samples present different pore sizes, the intrusion pressures of each sample are different; for sample 0 around 7 MPa, sample I around 27 MPa and sample II around 33 MPa. This increment in the intrusion pressure corresponds inversely to the pore size of the Si-monolith samples (Figure 54). This effect can be observed from the intrusion-extrusion curves at low compression/decompression rates (Figure 57) due to the sensibility of our PVT device is not enough to see the plateau of the pressure, *i.e.*, as the porosity layer is limited, the intrusion volume is very low.

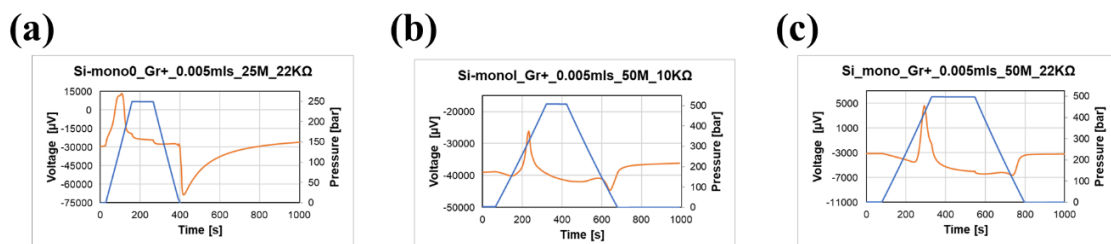


Figure 57.- Electrical signal (orange line) and pressure (blue line) of a compression–decompression test at $0.005 \text{ ml}\cdot\text{s}^{-1}$ for the monolith configuration of **(a)** sample 0, **(b)** sample I and **(c)** sample II.

After these preliminary analyses, the Si-monolith samples were subjected to intrusion-extrusion tests at 0.3 ml s^{-1} rate. The voltage and current peaks were observed for the samples (Figure 58). These peaks present a clear asymmetry between intrusion and extrusion, which could be due to the fact that the extrusion occurs slower for grafted porous monoliths.

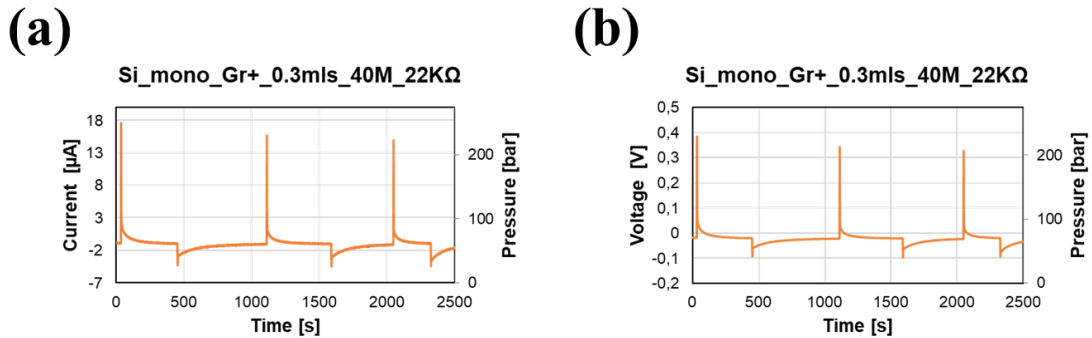


Figure 58.- (a) Voltage and (b) current signal with the peaks of intrusion/extrusion and pressure of a compression/decompression test at $0.3 \text{ ml}\cdot\text{s}^{-1}$ for sample 0 with the monolith configuration.

The corresponding resistance optimization was carried out for the different SI-monolith samples (Figure 59a), finding an optimal resistance of around $6 \text{ K}\Omega$ for the three samples. The power density (Figure 59b) was also obtained, in this case, the electrode surface was the area of the porous side of the Si-monolith sample.

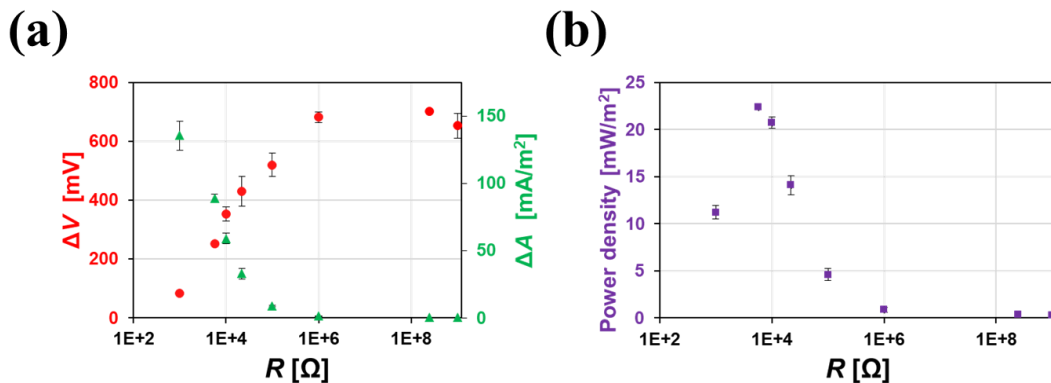


Figure 59.- (a) Current and voltage amplitudes and (b) power density at different electrical resistances in the circuit of the monolith configuration with sample 0.

When the energy of these three Si-monolith samples is compared, we obtain that sample 0 presents the highest values (Figure 60). This could be related to the fact that sample 0 has the highest pore volume of these samples (see Figure 54).

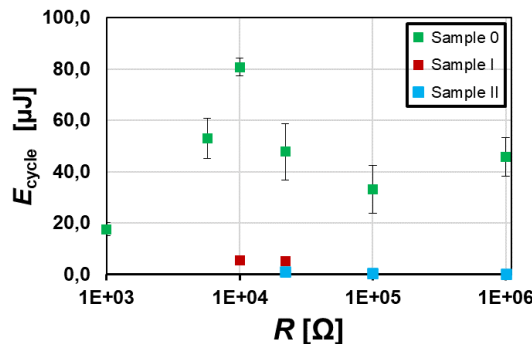


Figure 60.- Generated energy per intrusion-extrusion cycle for different Si-monolith samples at different electrical resistances.

Finally, the rate of compression/decompression was analysed finding an increment of 50 % in the energy per cycle when the rate increases from 0.3 ml s^{-1} to 0.7 ml s^{-1} (Figure 61). This effect was also found for other configurations and materials and it is important because the prototype tests will be carried out at high frequencies.

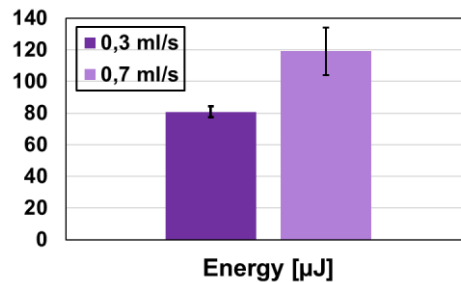


Figure 61.- Generated energy per intrusion-extrusion cycle for Si monolith sample 0 at different compression/decompression rates.

Moreover, the effect of different intrusion liquids was studied. In this case, a double-layered monolith with the following properties was used:

- Monolith V → Pore size (ϕ): 15.4 nm. Thickness: 31.8 μm

The liquids used were heavy water D_2O and a solution of polyethylenimine (CAS 9002-98-6) with a concentration of 1 mg/1 ml (PEI/water). The intrusion liquids, *i.e.* H_2O , D_2O and PEI sol., were encapsulated (see Figure 62a) and the Si-monolith was connected to the circuit using a gold wire attached to the Si-monolith using a conductive silver paste (see Figure 62b).

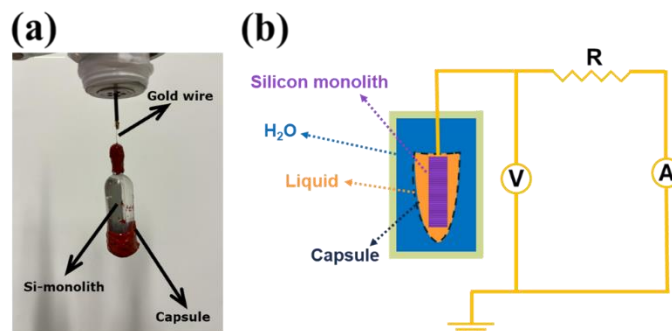


Figure 62.- (a) Si-monolith encapsulated and (b) schematic circuit for the encapsulated Si-monolith configuration.

The results for the compression–decompression cycles with the different liquids show a clear increment in the electrical out following this order; water, heavy water and PEI solution from lower to higher (Figure 63).

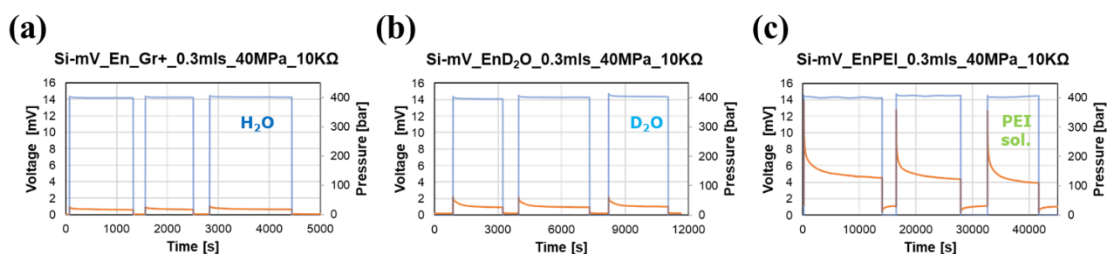


Figure 63.- Voltage during compression–decompression cycles for the encapsulated Si-monolith configuration with (a) water, (b) heavy water and (c) PEI solution.

Both the power density and the energy per cycle increase greatly, especially for the PEI solution (Figure 64). The power density doubled when changing from H_2O to D_2O , *i.e.* from 1.60 ± 0.08 to

$3.18 \pm 0.08 \mu\text{W}\cdot\text{m}^{-2}$ but when the liquid is the PEI solution the power density increases one order of magnitude to $68 \pm 4 \mu\text{W}\cdot\text{m}^{-2}$. In the case of energy per cycle, an increment of one order of magnitude is found for each liquid in the following order: H₂O with $0.017 \pm 0.005 \mu\text{J}$, D₂O with $0.110 \pm 0.005 \mu\text{J}$ and PEI solution with $7.0 \pm 1.3 \mu\text{J}$.

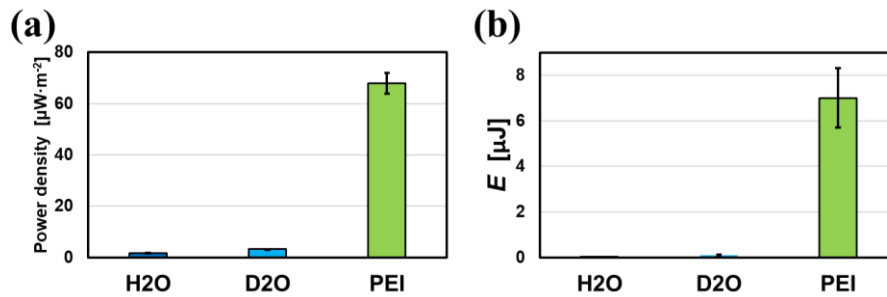


Figure 64.- (a) Power density and (b) energy per cycle for the encapsulated Si-monolith configuration with water, heavy water and PEI solution.

3.2.4. OTHER CONFIGURATIONS

Considering that degradation was found to be related to the applied bias voltage, a mitigation strategy was applied, the experimental configuration was switched to a single-electrode passive configuration, where no bias voltage was applied (Figure 65).

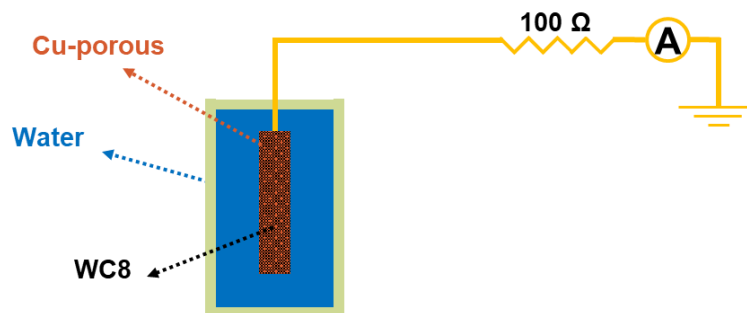


Figure 65.- Schematic circuit for the single-electrode passive configuration using a Cu-porous electrode and grafted silica C8-CH₃ as porous material.

Thus, a porous-copper strip was used as an electrode that was connected to the ground. The porous-copper strip was filled with a total of 1 g of the grafted silica C8-CH₃ (Figure 66a). Finally, this porous-copper electrode was wrapped in PTFE tape to keep the silica C8-CH₃ inside and connected to the external circuit to measure NTE (Figure 66b). Then, compression/decompression tests were carried out up to 300 bar.

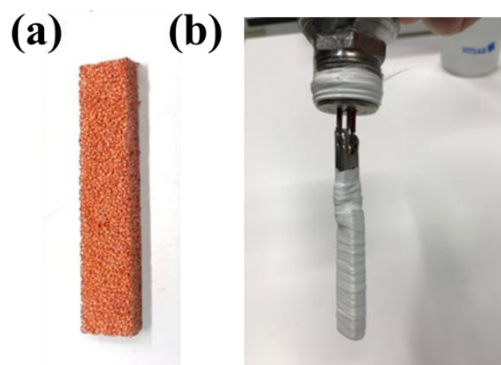


Figure 66.- (a) Porous-copper strip used as electrode and (b) how it was wrapped in PTFE tape and connected to the circuit.

The results show that current is generated (Figure 67) when the intrusion/extrusion occurs. Furthermore, the electrification peaks present in the opposite direction for intrusion and extrusion, which is in line with the literature for triboelectric-nanogenerators (TENGs). However, the electrical signal obtained for this single-electrode configuration was noisy and had low repeatability. Finally, the generated energy was very low, around $5 \cdot 10^{-7} \text{ J} \cdot \text{g}^{-1}$. This is in line with the previous experimental campaign for the double electrode scheme, where the application of bias voltage is beneficial to increase the electrical output.

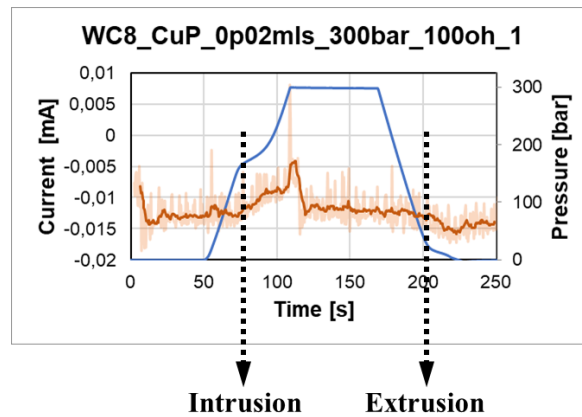


Figure 67.- Electrical signal (orange line) and pressure (blue line) of a compression/decompression test at 0.02 ml/s for the single-electrode passive configuration using a Cu-porous electrode.

Similarly, the porous copper monolith was filled with MOF ZIF-8 to study the triboelectrification effect. As previously, the porous-copper electrode was wrapped in PTFE tape to keep the porous material inside and connected to the external circuit to measure NTE (Figure 68). This configuration did not show a significant difference from previous results.

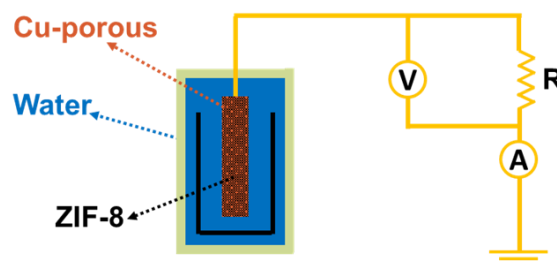


Figure 68.- Schematic circuit for the single-electrode passive configuration using a Cu-porous electrode and ZIF-8 as porous material.

As a new strategy to improve the single-electrode passive configuration (Figure 69), the geometry of the electrode was changed to gain contact surface between the electrode and the PM in an attempt to increase the charge transfer between them.

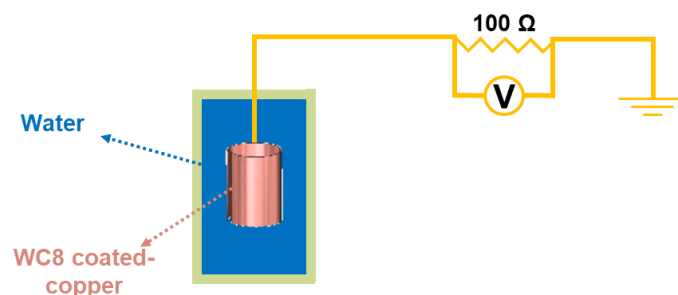


Figure 69.- Schematic circuit for the single-electrode passive configuration using a coated Cu-film electrode.

Therefore, a copper film was coated with 0.1376 g of grafted silica C8-CH₃. The silica was applied on the surface film mixed with a polymer (PVDF) and a solvent (DMF) which do not affect the structure of the silica. This mixture is used to ease the application by drop-casting of the silica on the surface film as well as to adhere it to the surface after the solvent evaporation during curing at 60 °C for 24 h. Then, the C8-CH₃-coated copper-film electrode was connected directly to the circuit (Figure 70). As in previous tests, compression/decompression tests were carried out up to 300 bar.

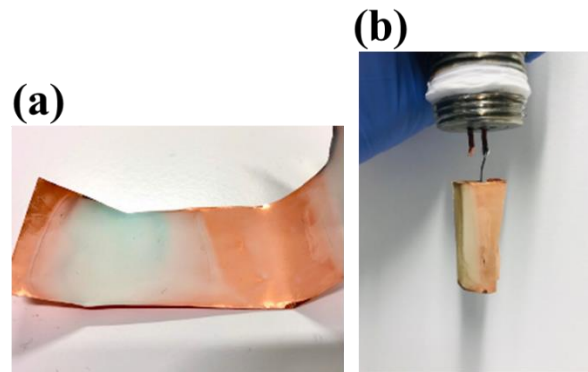


Figure 70.- (a) C8-CH₃-coated copper film used as electrode and (b) connection to the circuit.

Firstly, the intrusion–extrusion *PV*-isotherms of the coated film were analysed to ensure that the polymer does not block the nanopores. Then, comparing with raw silica C8-CH₃, it was found that the C8-CH₃-coated film keeps 90 % of the intrusion/extrusion volume (Figure 71).

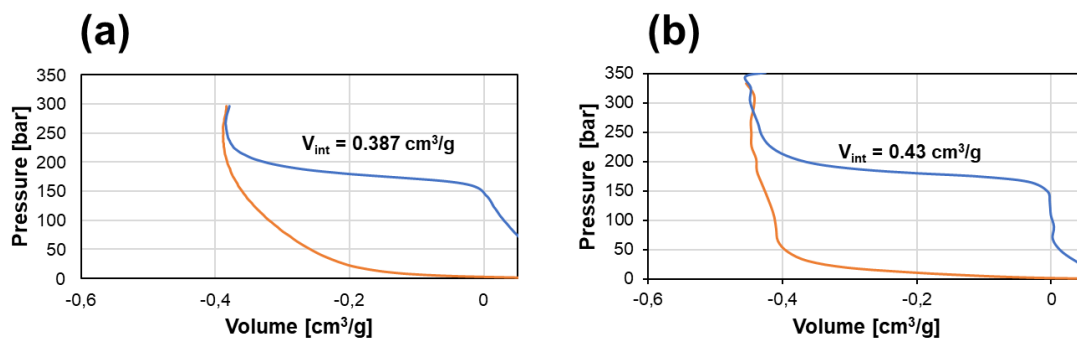


Figure 71.- (a) Intrusion/extrusion isotherms of C8-CH₃-coated copper film and (b) intrusion/extrusion isotherms of raw grafted silica C8-CH₃.

However, no electrification during intrusion–extrusion of water into C8-CH₃-coated film was evident (Figure 72).

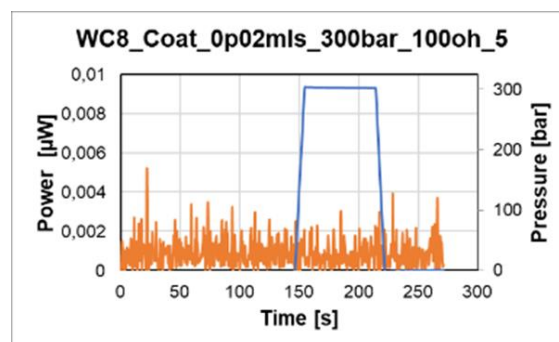


Figure 72.- Electrical signal (orange line) and pressure (blue line) of a compression/decompression test at 0.02 ml/s for the single-electrode passive configuration using C8-CH₃-coated Cu-film electrode. No electrification was observed during intrusion-extrusion cycling.

To understand why no electrification was found, the coated film was analysed by SEM (Figure 73) where it is found that the polymer used to maintain the grafted silica C8-CH₃ on the Cu-film surface had migrated from the external face to the internal one, insulating the electrode from silica C8-CH₃. This appears to be the reason for no electrification.

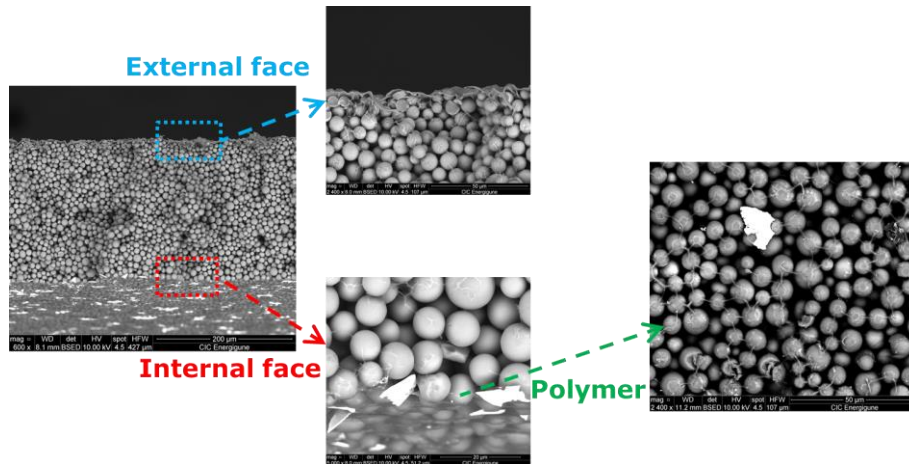


Figure 73.- SEM images of the C8-CH₃-coated copper film where the migration of the cover polymer is observed.

Another configuration that allowed to investigate the effect of the insulation of the electrode/porous material from the measuring vessel was explored (Figure 74). In this case, a dielectric oil was used as means of insulating the cell from the PM and water.

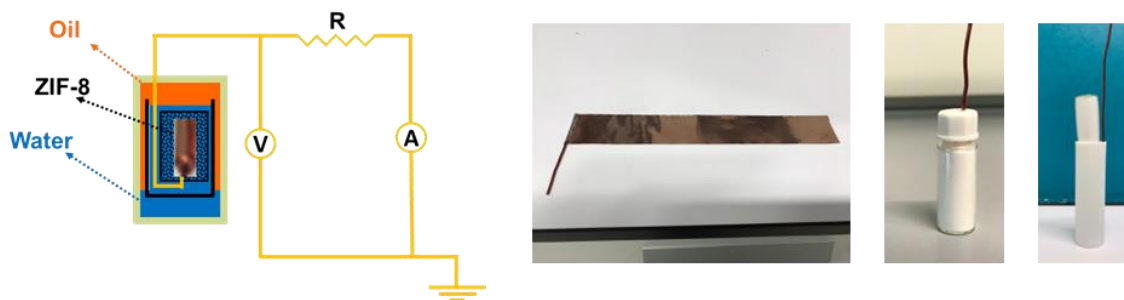


Figure 74.- Schematic circuit a configuration using oil to insulate the porous material and the film electrode inside a glass bottle.

But, as it can be seen in Figure 75, no triboelectrification effect was recorded in this configuration.

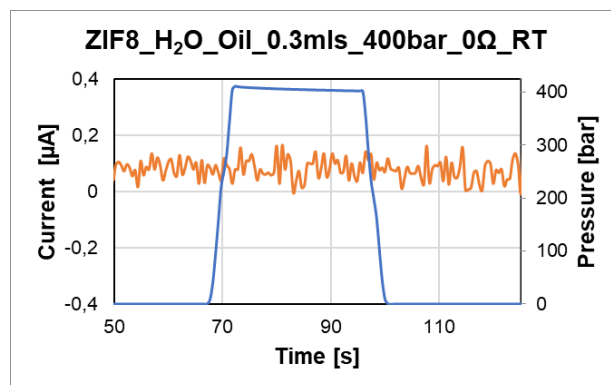


Figure 75.- Electrical signal (orange line) and pressure (blue line) of a compression/decompression test at 0.3 ml·s⁻¹ rate for the oil configuration. No electrification was observed during intrusion–extrusion process.

Apart from these main configurations, some alterations in the electrical circuit, in the encapsulation and in the type of electrodes were analysed to see the effect on the nanotriboelectrification of our system and decide the configurations to test. For example, the counter electrode of the passive configuration was located outside the measuring vessel (Figure 76a), also this external electrode was put inside of water at room temperature and hot water (around 80 °C) to see the thermal effect in the electrical output. Different connections of the passive scheme were also tried to study the effect on the electrical performance, *e.g.* see Figure 76b.

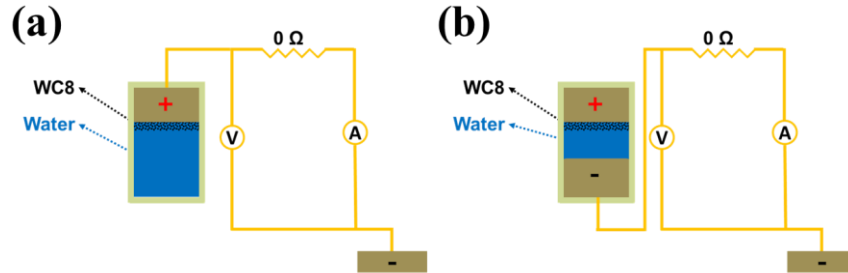


Figure 76.- Schematic circuits **(a)** with the counter electrode outside of the measuring vessel and **(b)** alternative connection to the log circuit.

As can be seen in Figure 77, no triboelectrification effects were detected during the intrusion-extrusion process using the electrical schemes depicted in Figure 76.

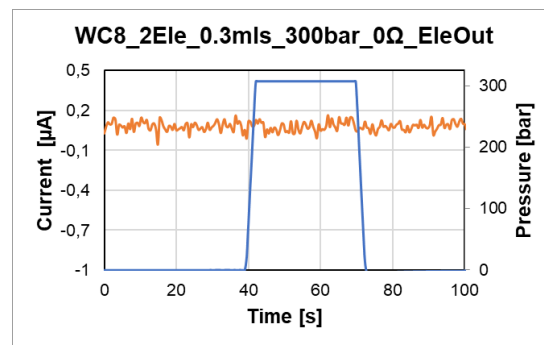


Figure 77.- Electrical signal (orange line) and pressure (blue line) of a compression/decompression test at 0.3 ml·s⁻¹ rate for the double-electrode passive configuration using an external counter electrode. No electrification was observed during intrusion-extrusion cycling.

3.2.5. SUMMARY OF RESULTS

To sum up all the obtained results for electrification and to compare them with literature results for other triboelectric generators, a figure of merit (FOM), which was proposed by Basset et al.⁹, was used. This FOM is defined as follow:

$$\text{FOM} = \frac{P}{f \cdot V_b^2 \cdot A} \quad (1)$$

Where P is the power density, f is the frequency, V_b is the applied bias voltage for active configurations and A is the electrode area Table 3 summarizes our results for all configurations and some results from the literature. As it can be seen, the performance of our system when a bias voltage is applied is far greater compared to the state-of-the-art. Bear in mind, however, that when a bias voltage is applied, the stability and the kinetics of the porous material need to be improved. The passive configurations (without bias voltage) do not have problems with materials degradation and demonstrate improved kinetics of discharging, however, the energy output needs to be further optimized.

Table 3.- Comparison of different nano-tribogenerators and their power generation.

Power density [$\mu\text{W}/\text{m}^2$]	Voltage [V]	Frequency [Hz]	FoM ⁹ [[$10^3 \cdot \mu\text{W}/\text{mm}^2 \cdot \text{Hz} \cdot \text{V}^2$]]	Type	Reference
924	8	250	$5.8 \cdot 10^{-5}$	Electrostatic	Basset et al. ⁹
$100 \cdot 10^6$	60	2	13.9	Electrowetting	Krupenkin et al. ¹⁰
$100 \cdot 10^6$	4.5	300	16.5	Electrowetting	Hsu et al. ¹¹
960	1.2	6	0.1	Electrowetting	Huynh et al. ¹²
$110 \cdot 10^6$	24	3	63.4	Electrowetting	Yang et al. ¹³
$38.2 \cdot 10^6$	6	4	265.27	NTE	Liu et al. ¹⁴
533	0.01	3	1776.7	Electrowetting	Adhikari et al. ¹⁵
30	0	10	∞	Electrowetting	Kim et al. ¹⁶
$3 \cdot 10^6$	4	Quasistatic	35456	NTE	^a This work
38	0	Quasistatic	∞	NTE	^b This work
115	0.5	Quasistatic	260.4	NTE	^b This work

^a Configuration depicted in Figure 27a

^b Configuration depicted in Figure 27b

Finally, summarizing all the configurations and materials during the project, the progression in achieved power density can be tracked. This increment is of almost two orders of magnitude for the different materials with the passive configuration but comparing with the monolith configuration the increment is of three orders of magnitude (Figure 78). It is of highest importance to note that the tested monolith is not yet optimized. It has very thin $\sim 30 \mu\text{m}$ porous layer. It is expected to increase the electrification dramatically by increasing the thickness of this layer.

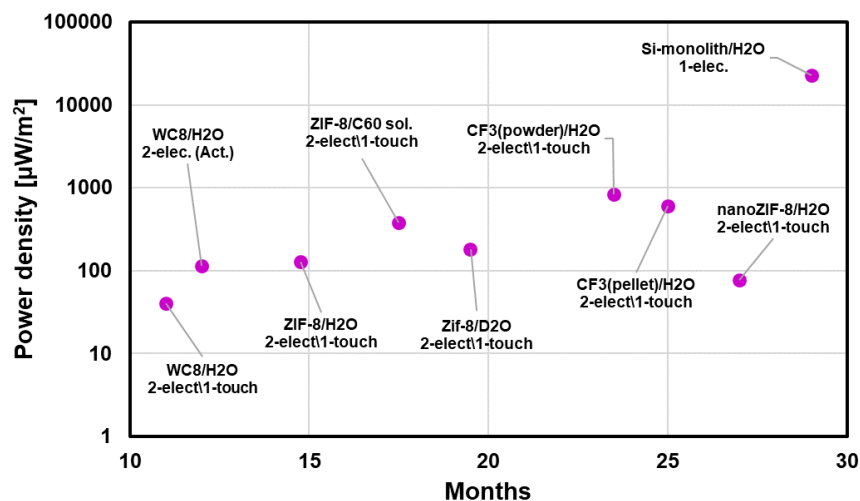


Figure 78.- Progression of the power density per intrusion-extrusion cycle for different materials and configurations.

4. DEVELOPMENT AND VALIDATION OF NANOTRIBOELECTRIFICATION MODEL

The origins of nanotriboelectric charging have been subject to extensive debate in the literature, encapsulated in a recent overview of contact electrification¹⁷, and has taken on new importance considering the potential energy-recovering nanotriboelectric generators. The debate governing the charging of surfaces upon contact with a liquid is framed between two mechanisms, electron or ion transfer. Understanding the underlying physical drivers of nanotriboelectrification in the context of triboelectric generators is essential to maximise the charge quantity transferred between the liquid and solid, to maximise the potential difference generated upon separation of contact. Most current literature centres on solid-solid triboelectrification, with limited bibliographic data to use to drive maximisation of liquid-solid contact electrification. Moreover, our electrification is taking place between the internal area of a porous material and a confined liquid as opposed to conventional planar interfaces. This poses additional challenges: i) curved surfaces show peculiar effects¹⁸ but their understanding is still highly limited and restricted to solid/solid interfaces; ii) Confined water has different characteristics with respect to bulk ones. Finally, iii) it is unclear whether the design features that advantage electrification may create barriers to intrusion or extrusion; for example, tight contact between liquid and solid might be incompatible with the high hydrophobicity necessary to allow intrusion–extrusion cycling.

Recent studies have favoured electron transfer upon contact as the dominant process governing triboelectrification¹⁹. Studies into solid-solid electrification have proposed the presence of localised gap states, typically associated with surface “dangling bonds” or surface reconstruction to be responsible for electron transfer^{17,20,21}(see Figure 79). When a donor material is brought into tight contact with a suitable acceptor one, the potential barrier to transfer is significantly lowered and electrons can transfer from the former to the latter. Increasing the contact surface area should increase the number of donor and acceptor states brought into contact, and therefore the quantity of charge transferred. Porous materials have an area density much larger than their counterpart, ranging from hundreds to several thousand square meters per gram of material. Of course, the partner system of a porous material cannot be a solid as it cannot enter into contact with the internal area of the material. However, contact electrification is not limited to solids: triboelectrification occurs between any pair of materials, *e.g.* liquid-solid. However, in this case, the mechanism behind the observed contact transfer has still to be established.

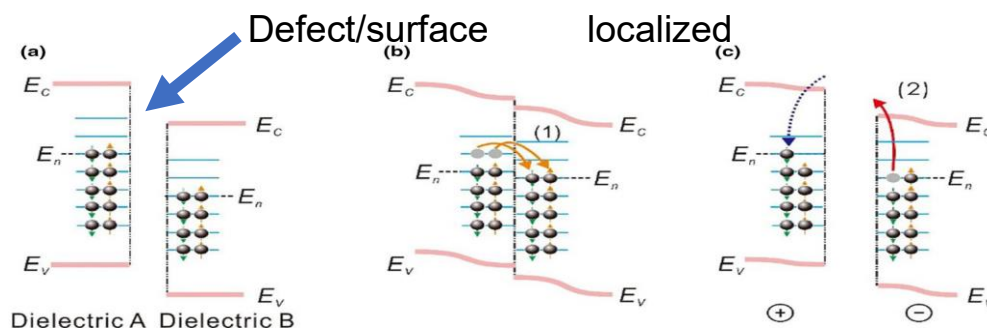


Figure 79.- Scheme of the mechanism of contact electrification between two dielectrics before contact (left), in contact (centre) and after contact (right), illustrating electron transfer in the instance that dielectric B's acceptor level potential is lower than the donor level of dielectric A. Similar schemes hold for dielectrics in contact with molecular systems, *e.g.* liquids¹⁷.

Two porous materials combining the desired intrusion-extrusion cycle and a large internal surface area favouring charging events are zeolitic imidazolate framework 8 (ZIF-8) and grafted silicas, in this project, grafted with hydrocarbons, typically of length 8 carbon atoms C8-CH₃ and with its fluorinated analogue C8-CF₃. The MOF ZIF-8, a porous framework of tetrahedrally coordinated Zn²⁺ ions connected via methyl-imidazolate linkers, has a large internal surface area (1800 m²·g⁻¹) intruding at 25 MPa^{22,23}. The grafted silica C8-CH₃ likewise possesses 400 m²·g⁻¹ of internal surface area and undergoes intrusion at a slightly lower pressure, 17 MPa²². Both materials have shown experimental evidence of electrification (see Section 3.2.2). But, in pristine condition, ZIF-8 should not contain gap states as it presents no undercoordinated surface atoms and has no distortion of bonds from surface reconstruction. Meanwhile, the silica surface in theory has gap states, but the grafted hydrophobic chains in C8-CH₃ should prevent any possibility of water-silica surface contact and disallow electron transfer directly between the liquid and inorganic solid. To reconcile the apparently contradictory nature of observed charging with ZIF-8 that by design should offer no route to charging, we suggest the presence of linker (V_{lm}^*) and Zn defects (V_{zn}'') as potential sources of undercoordination. These defects may be pre-existing or be formed upon intrusion. Meanwhile, for C8-CH₃ we investigate the possibility that i) charge transfer occurs between the liquid and the grafting molecules, ii) that despite grafting, liquid enters in contact with a-SiO₂ and exchanges electrons between them, and iii) grafting defect, effectively creating a hydrophilic patch allowing the water to reach the surface.

To test our theory of electron charge transfer for both systems, we faced the challenge of sampling the multiple configurations the systems can take, especially the grafting molecules, requiring multiple nanosecond timescales, beyond reach for *ab initio* simulations necessary to investigate processes involving electrons. This is reconciled with a multi-scale hierarchical approach, in which classical molecular dynamics are employed to allow nanosecond-scale simulation, wherefrom *ab initio* scans/shortened trajectories can be performed. The tailoring of this methodology to our individual ZIF-8 and grafted silica systems will be expanded upon in Section 4.1. As shown Figure 80, one can separate the solid and liquid components of the simulated system and calculate the individualised electronic densities, in this example, C8-CH₃ and H₂O. This approach confers two essential tools to evidence electron transfer. Firstly, a means of calculating charge transfer via Bader analysis, which uses maxima and minima in the electronic density field to assign charge to individual atoms within our molecular system²⁴. One can take the difference in charge assignment between the whole system $\rho\{\text{PM}+\text{H}_2\text{O}\}$ and the separated components, *i.e.* the porous material (PM) and H₂O densities denoted ρ_{PM} and $\rho_{\text{H}_2\text{O}}$ respectively, to identify charge transfer between the two, and calculate the net transfer as:

$$\Delta\rho = \rho\{\text{PM} + \text{H}_2\text{O}\} - (\rho_{\text{PM}} + \rho_{\text{H}_2\text{O}}) \quad (2)$$

This therefore permits a quantifiable measure of charge transfer to indicate net direction of charge, in addition to being able to visualise areas of apparent charge transfer.

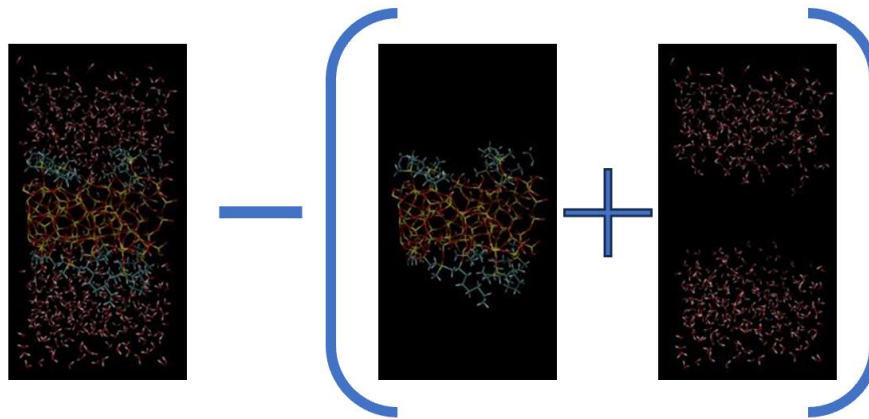


Figure 80.- Cartoon illustrating the calculations to determine electronic charge transfer via the difference of electronic density of the entire system (left) and solid (centre) and liquid (right) subsystems sampled by molecular dynamics.

Separation in subsystems and calculations of their density of states (DOS) assist us in understanding the contact electrification mechanism once solid and liquid are brought into contact. DOSs have proved very useful in identifying potential electron transfer routes where charge partitioning offers a limited picture, particularly in the {grafted silica + H₂O} system study, as will be expanded upon in Section 4.1.

We have also initiated work to look at the feasibility of ionic charging routes in the grafted silicas systems, *i.e.* {C8-CH₃ + H₂O} and {C8-CF₃ + H₂O} systems. The proposal is that the ionic grafting species sticking to the internal walls of the porous material left from defect creation could remove an H⁺ or OH⁻ from a water molecule to neutralise, leaving behind ions in the water bulk that would be extruded, promoting charge separation with the complementary defect on the silica. We have proposed a similar bespoke multiscale methodology to evaluate the feasibility of ionic charge transfer routes, which we outline in more detail in Section 4.2.

4.1. MODEL OF NANOTRIBOELECTRIFICATION VIA ELECTRONIC CHARGE TRANSFER

4.1.1. {ZIF-8 + H₂O} CASE

Herein, we have centred on ab initio molecular dynamic simulation to assess the hypotheses of ZIF-8 contact electrification. We considered a perfect crystalline (276 atoms per unit cell) sample and the most likely defects, which, according to Zhang et al.²⁵, are zinc and methyl imidazolate vacancies, V_{Zn}'' and V_{Im}^* respectively. Indeed, at a variance with the other samples, V_{Zn}'' demonstrates the presence of gap states (Figure 81a). Crucially, these states are in the energy range of bulk water, making this defect a prime candidate for electron transfer (Figure 81b).

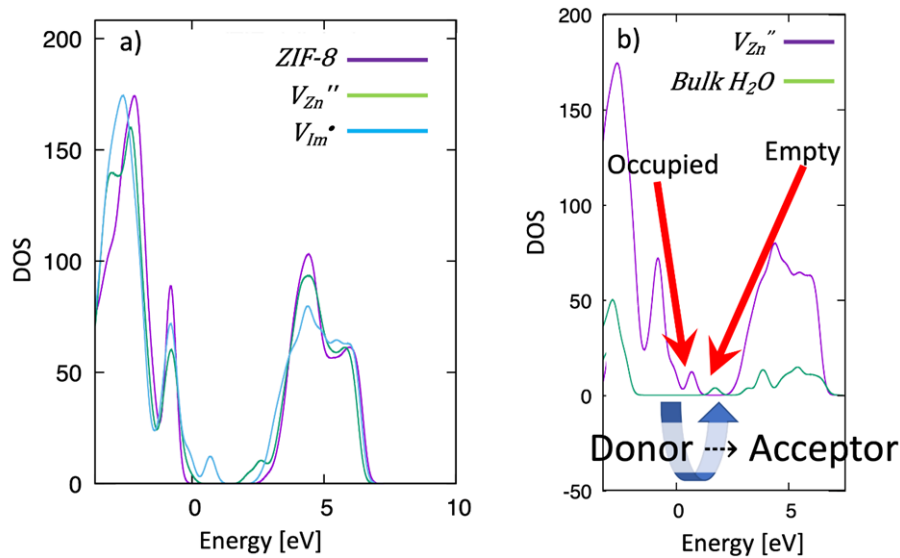


Figure 81.- Density of states of V_{Zn}'' ZIF-8 (purple) and bulk water (green). The ZIF-8 gap states are in close proximity to those of the bulk water acceptor states. This contrasts with perfect and V_{Im}^* , which have no bandgap states.

Of course, the highly confined water filling ZIF-8 cavities might have a different electronic structure, and the same is true for intruded ZIF-8. To address this question, we consider simulations of water-intruded defected and pristine ZIF-8. Simulations were each run for 10 ps, with two levels of intrusion considered for each system, 35 and 40 water molecules/cage, filling values determined from classical molecular dynamics simulations ran in the context of the WP3. We considered two filling levels to investigate the effect of over-pressurization, *i.e.*, applying a pressure higher than the end of the intrusion plateau of the PV -isotherm. Moreover, two values of the lattice parameter, the equilibrium value and a value larger by 0.06 Å, correspond to the experimental expansion measured by neutron diffraction experiments by experimental project partners²³.

It is well-known that the concept of atomic charges is ill-posed but of highly practical value; Thus, one typically resorts to an arbitrary but unique definition of atomic charges. To this end, we decomposed electron density via the so-called Löwdin population analysis²⁶ to identify notable charge transfer and its localisation. We also considered a second approach based on the composition of the electron density via the so-called Bader charges²⁴. In particular, we selected several configurations from *ab initio* MD and for these, we computed the electron density of the entire sample and the ZIF-8 and water subsystem: $\Delta\rho = \rho_{ZIF-8/H_2O} - (\rho_{ZIF-8} + \rho_{H_2O})$. From the difference of the Löwdin/Bader charges obtained from the entire and subsystems one obtains the amount of charge transferred. For the 35 water molecules per cage, the sample containing the V_{Zn}'' defect reported a decrease of electron density on the ZIF-8 by 0.7 electrons (Table 4), approximately twice the values measured for the pristine sample and the one containing V_{Im}^* . This charge is highly localized, as shown in Figure 82.

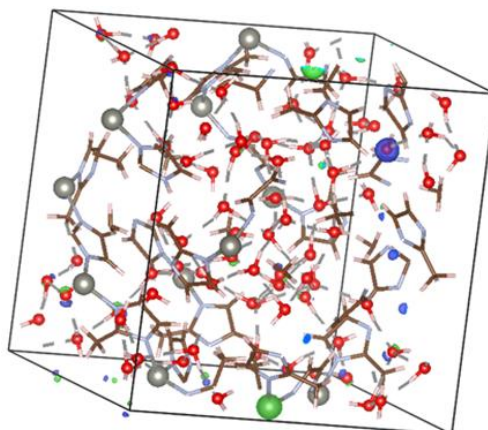


Figure 82.- Plot of the density variation $\Delta\rho$ showing that excess charge (of opposite sign) is localized on the framework and an individual water molecule laying in a pseudo-hexagonal window connecting neighbouring ZIF-8 cavities.

For the stretched ZIF-8 sample, charge transfer grows in all cases, with the charge transfer of the pristine samples reaching the same value of the V_{Zn}'' case, $\sim 1.05 < e$ (Table 4). This suggests that upon intrusion the stretching of ZIF-8 favours charge transfer from water to ZIF-8 in all cases, but in the presence of V_{Zn}'' the transferred charge is better retained due to the presence of localized defect states.

Table 4.- Charge accumulated on pristine and defected ZIF-8. Two values of the lattice parameters have been considered, 17.004 Å, the equilibrium value for the empty system, and 17.064 Å, the value after the 0.06 Å expansion upon intrusion.

System	q17.004 Å [e]	q17.064 Å [e]
Bulk	0.42 ± 0.01	1.1 ± 0.1
V_{Im}^o	0.4 ± 0.2	0.7 ± 0.2
V_{Zn}''	0.70 ± 0.04	1.1 ± 0.06

Indeed, the observed expansion upon intrusion²³ might play a role in the formation of defects, whether they have positive effects on contact electrification or diminish the stability of the porous material. We performed energy vs lattice parameter calculations to identify the equilibrium value for the pristine and defected systems and found that the value in the presence of V_{Zn}'' is larger while in the presence of V_{Im}^* is smaller, suggesting that intrusion, and the ensuing expansion, may induce the formation of zinc vacancies.

We then performed population analysis on the two cell sizes, we reported the Bader-charge-determined charge transfer for standard intrusion pressure filling, as summarised in Table 4. We identified the strongest charge change as that of V_{Zn}'' at standard cell size, which we were able to visualise in Figure 82 as a highly localised charge transfer, corresponding to a loss in the vicinity of the missing Zn^{2+} and transfer onto a water molecule in the vicinity of the pore aperture. Meanwhile, charge transfers due to V_{Im}^* was reported to be effectively that of the pristine ZIF-8 cell. Charge transfer was then magnified in the case of the expanded cell for all three ZIF-8 cells studied, with a change in transfer direction, here water lost charge to the expanded ZIF-8 cell, suggesting intrusion may play a role in water-ZIF-8 transfer.

Calculations of defect formation energy reveal that cell expansion favours their formation, suggesting an overall positive feedback mechanism: expansion favours the formation of defects, in particular, expansion favours the formation of V_{Zn}'' , and defects favour electron transfer. Whether this process continues along many intrusion cycles, leading to a complete degradation of the porous material.

4.1.2. {GRAFTED SILICA + H₂O} CASE

For grafted silica, we opted to study both C8-CH₃, that already been considered in previous experimental works on intrusion-extrusion contact electrification and by our experimental partners, and C8-CF₃, the fluorinated analogue, motivated by recent literature²⁷ that suggested a strong triboelectric effect for silica grafted with fluorinated carbon chains. What remained unclear from the literature was whether the chains themselves played a role in charge transfer, or whether it was exclusively governed by changing the accessibility of water to a-SiO₂ surface^{2,27}.

Upon testing of a model grafted C8-CH₃ slab exposed to water, it became clear that the ps-timescale accessible by *ab initio* simulations is insufficient for a satisfactory sampling of the probability density of the minimalistic still complex system illustrated in Figure 83. To bring this difficulty into relief, while retaining the necessary information garnered by *ab initio* simulation, a multi-scale hierarchical approach was taken, to generate configurations from a 20 ns classical molecular dynamics simulation. *Ab initio* scans were then performed on the entire system, then the separated solid and liquid components, directly from these configurations. It is worth remarking that, to the best of our knowledge, no force fields are available to model C8-CH₃ or C8-CF₃. Building of a bespoke force field took off-the-shelf parameters for the amorphous SiO₂ bulk from Emami et al²⁸. For the grafting chains, we used the OPLS-AA force field²⁹ with 1.14*CM1A charges^{30,31} and benchmarked on a single chain grafted to the surface comparing MD with *ab initio* results. Simulations were performed on a 402-atom a SiO₂-slab, periodic in the *x* and *y* directions, with grafting performed on the two exposed surfaces orthogonal to direction *z*, which were exposed to 512 water molecules (see Figure 83). Grafting density was set to 1.3 chains-nm⁻², the maximum without overlaps between chain electronic densities, a problem for fluorinated chains with longer C-F bond lengths.

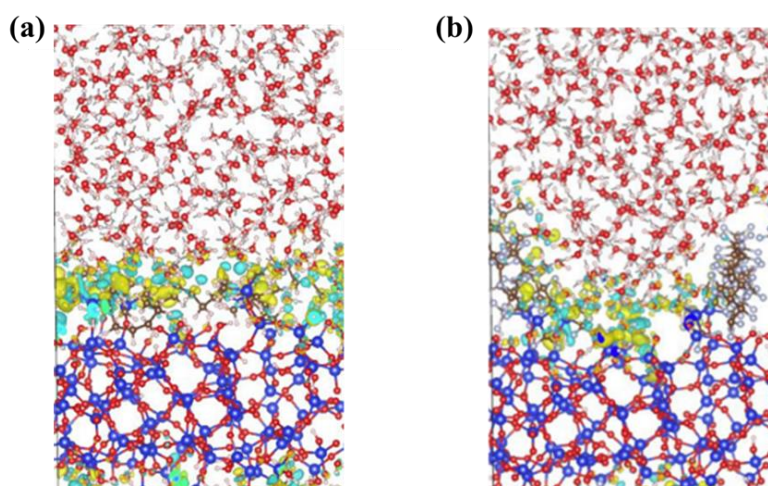


Figure 83.- Visualisation of charge differences calculated for **(a)** C8-CH₃ and **(b)** C8-CF₃ when solvated in H₂O (yellow represents charge gain and blue charge loss. Isovalue 0.001). This graphic illustrates strong differences between the C8-CH₃ and C8-CF₃ chains alluded to in the text. C8 chains are highly flexible and fold to cover the SiO₂ surface, preventing SiO₂ surface–water contact. C8-CF₃ chains are increasingly rigid, leaving larger uncovered gaps between grafting chains, allowing contact between water and the silica surface, in a range in which charge transfer can occur.

We initially focused on the behaviour of the fully grafted C8-CH₃ and C8-CF₃ in contact with water. Seeing Figure 83, one observes a difference in behaviour between C8-CH₃ and C8-CF₃. C8-CH₃ chains are very flexible and fold relatively quickly, within picoseconds in simulations, forming a form of “canopy” over the amorphous SiO₂ surface, while C8-CF₃ chains are more rigid and remain more vertical, creating more spatial gaps through which water molecules can arrive

at the amorphous SiO₂ surface. Figure 83 shows charge density difference as in Eq. 2. Charge transfer results as obtained from Bader charge analysis are summarized in Table 5 across both fully grafted systems. There is a switch in the electron transfer direction observed between both systems, water becomes more negative, picking up charge from C8-CH₃, while appears to lose charge to C8-CF₃. Breaking down the charge transfer between the chains and silica surface, one observes that this change in polarity is entirely driven by the chain electron transfer. The C8-CH₃ chain loses electron charge by nearly 0.15e on average, while C8-CF₃ extracts -0.45e from the water. There is a slightly stronger interaction between the surface and water for C8-CF₃ grafting silica with respect to C8-CH₃ (increase from -0.04e transferred to the surface to -0.06e), apparently due to the lack of canopy formed over the C8-CF₃-grafted surface.

Table 5.- Charge transfer calculated between the fully-grafted SiO₂ and water molecules, further broken down into charge transfer between water molecules and the C8-CH₃/C8-CF₃ chain and SiO₂ surface components via atom-in-molecule partitioning (Bader charges). One notes a directional shift in charge transfer direction driven by the chains.

System	H2O Overall $\Delta q/e$ (SD)	Chain $\Delta q/e$ (SD)	SiO2 $\Delta q/e$ (SD)
{C8-CH ₃ + H ₂ O}	-0.103 (0.041)	+0.147 (0.038)	-0.043 (0.042)
{C8-CF ₃ + H ₂ O}	+0.520 (0.041)	-0.458 (0.035)	-0.062 (0.026)

However, one must be careful in the interpretation of Bader charges. Indeed, charge partitioning can be influenced by instantaneous polarisations when atoms are in contact, while does not result in permanent charge transfer but is rather a polarization of molecules. To try to distinguish between polarization and net charge transfer, which can persist after extrusion, we analysed the density of states (DOSs) of the various systems. A quick glance at Figure 84a, corresponding to fully grafted C8-CH₃ and C8-CF₃, reveals no gap states, with a clean separation of occupied and unoccupied orbitals. Even the highest occupied molecular orbitals on the C8-CH₃ and C8-CF₃ correspond to undercoordinated parts of the amorphous SiO₂ structure, rather than the chains. This appears to identify the water-chain interaction as polarisation, as opposed to permanent charge transfer.

Having appeared to rule out the chains as playing a role in “permanent” charge transfer, we renew our focus on defects in the grafting as a driver to increase interaction between water and the SiO₂ surface. To this end, we removed a single chain, one in the centre of our periodic slab, on one of the two surfaces of the slab. We consider two possibilities, a chain cut at the Si-O bond connecting the chain and surface, leaving a O⁻ defect exposed on the surface, and a second cut where the O⁻ goes also with the chain, leaving an exposed Si⁺ defect. Considering the grafting defect leaving behind O⁻ on the surface, the molecular dynamics shows coordination of the defect into a local cluster of water molecules, whose positive poles orient toward the surface anion. Figure 84b displays the DOS for the system with the O⁻ defect; One sees the appearance of a donor state on the silica surface for both chain types, C8-CH₃ and C8-CF₃, centred on the defect. This is complemented by the appearance of one or two acceptor states in water molecules coordinating within 2 Å of the defect of C8-CH₃ and C8-CF₃, respectively. When we consider the Si⁺ defect (Figure 84c), we have an apparent inversion of this process, with water gap donor states (one for C8-CH₃, three for C8-CF₃) corresponding to those waters close to the defect. There also appears to be the growth of a very small acceptor state, just before the bulk of the SiO₂ unoccupied orbitals, centred around the Si⁺ site. This is a potential driver of electron transfer from the water to the defect.

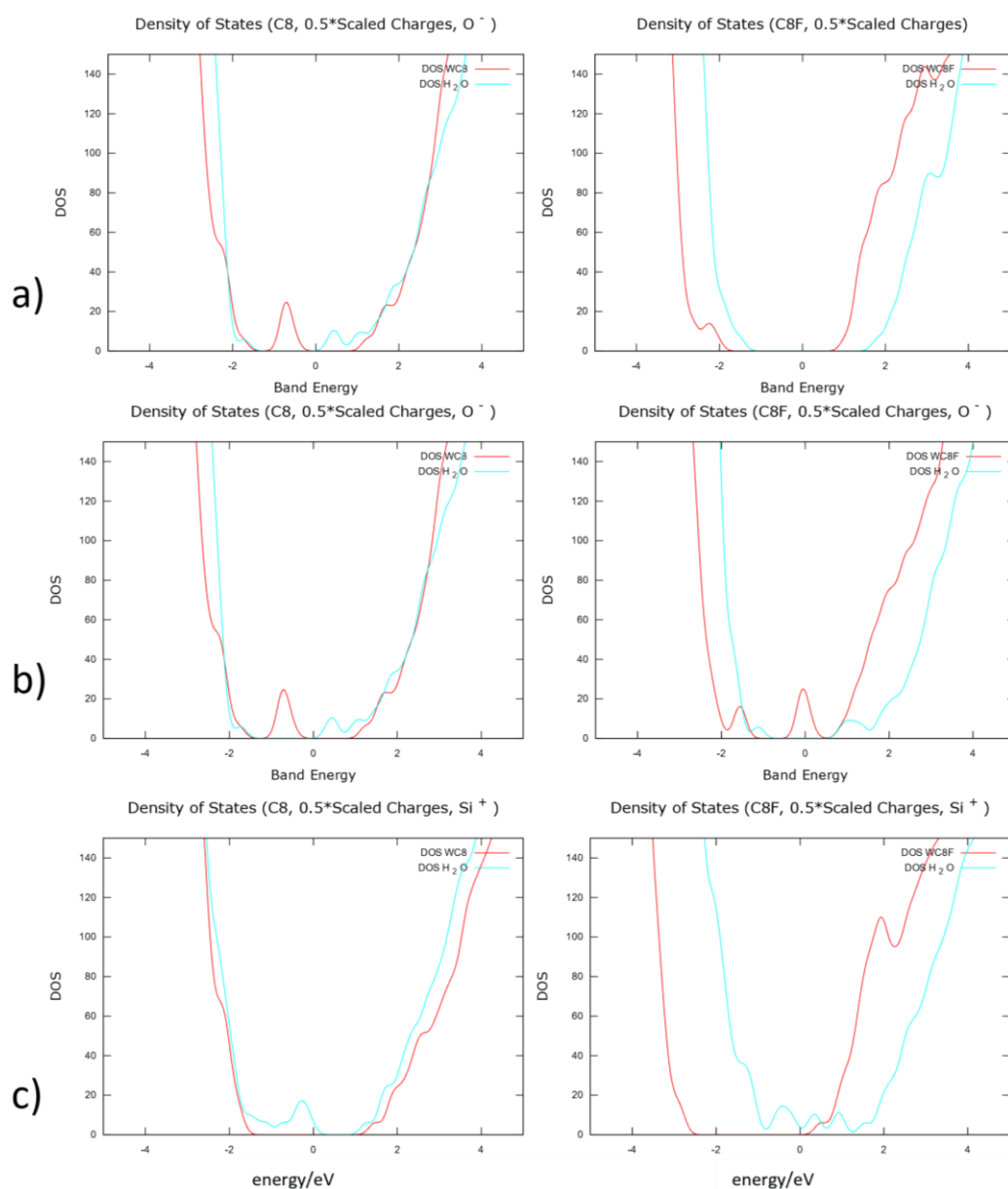


Figure 84.- Density of states (DOS) for C8-CH₃ (left) and C8-CF₃ (right) grafted silica. In red are reported DOSs of the solid and in cyan the ones of water. In the first row, panel (a) we report data for pristine grafted silica. In panel (b) data are reported for a grafting defect obtained by removing a Si⁺ terminated chain. In panel (c) we report corresponding data for a grafting defect corresponding to the removal of a O⁻ terminated chain.

This electron transfer study supports thus far the notion of grafting defects in both hydrocarbon and fluorinated counterparts as the origin of potential electron transfer routes in systems that do not otherwise exhibit charging. This is consistent with the observation that defects, namely Zn²⁺ vacancies, as a potential electron transfer driver in the otherwise perfect internal surface of ZIF-8.

4.2. MODEL OF NANOTRIBOELECTRIFICATION VIA IONIC CHARGE TRANSFER

Recently we have begun our evaluation of potential ionic charging routes to charge separation. Indeed, ionic charging routes have been shown to contribute to triboelectrification¹⁷. The first remark is that unattached grafting chains stick to the other grafting molecules still covalently bonded to the surface. This is consistent with DSC measurements revealing that unreacted grafting molecules do not get washed away during preparation. Hydrocarbon and fluorinated

chains resulting from the formation of defects retain an ionised tip, positive or negative, from their break with the silica surface (see Section 4.1.2). This has led to our proposal of two possible ionic charging routes, as illustrated in the schematic in Figure 85. One route is that a chain with a Si^+ tip (leaving the O^- defect on the surface) seeks neutrality by binding to OH^- from a water molecule, leaving an H^+ in the water bulk to be extruded. Alternatively, an O^- tip (responsible for the Si^+ defect on the surface) dissociates H_2O , bonding with an H^+ and leaving a dissociated OH^- in the water bulk. In practice, $\text{CH}_3(\text{CH}_2)_7\text{Si}(\text{CH}_3)_2^+$ and $\text{CH}_3(\text{CH}_2)_7\text{SiO}(\text{CH}_3)_2^-$, or the fluorinated counterpart, maybe less basic or acid of water, respectively. In this case, upon extrusion one produces the charge separation based on triboelectric nanogenerators.

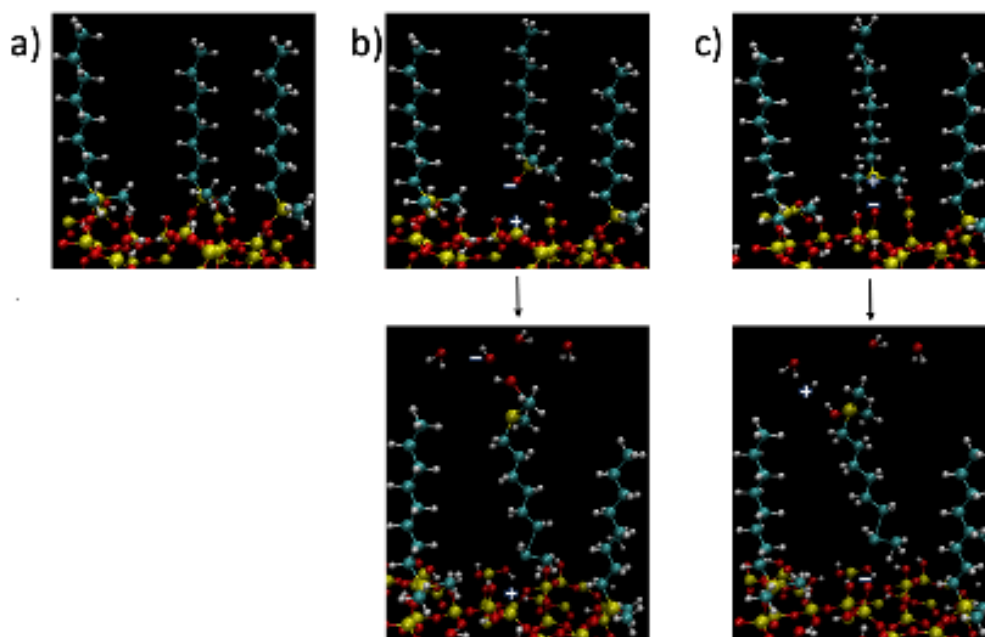


Figure 85.- Schematic outlining the possible mechanism of ionic charge transfer. In the (a) initial step, a (charged) grafting defect is located by removing a (b) O^- terminated or (c) Si^+ terminated chain. Our simulations revealed that the detached molecule reorientated, exposing the charged species toward bulk water. In the final step, the charged molecule can take H^+ or OH^- from water, depending on the relative acidity of the species.

To test both routes we have returned to a multiscale approach: extensive classical MD is run to sample the configuration space, followed by short *ab initio* MD starting from configuration extracted along the classical trajectories to allow electronic polarization and, when possible, chemical reactivity. However, proton or hydroxyl transfer from water to the grafting molecules may imply crossing a free energy barrier³², requiring a time exceeding the one accessible by simulations. Since one of the more immediate objectives for the Electro-Intrusion project is to investigate the viability of this mechanism, hence we will focus on the relative acidity and basicity of $\text{CH}_3(\text{CH}_2)_7\text{Si}(\text{CH}_3)_2^+$ and $\text{CH}_3(\text{CH}_2)_7\text{SiO}(\text{CH}_3)_2^-$, and the fluorinated molecules, by computing the relative energy with the neutralized counterpart produced by displacing OH^- or H^+ from a neighbouring molecule and relaxing the system.

5. CONCLUSIONS

This deliverable reports the progress of the Electro-intrusion project in understanding the contact electrification in the intrusion-extrusion cycle and strategies to maximize it.

The main experimental conclusions are as follows:

1. Materials:
 - a. Different types of materials were tested for water intrusion-extrusion and all of them demonstrate electrification phenomena. In particular, silica with different grafting, ZIF-8 metal organic framework and nanoporous silicon monolith were tested.
 - b. Grafted silica was chosen for the shock absorber prototype as demonstrates the best balance between stability, vibrations dissipation capability and electrification.
 - c. The stability of the chosen material was tested for 150 cycles without any loss of performance. It is expected to be tested over thousands of cycles at the prototype level as part of WP4.
 - d. Different liquids were tested. In particular, it has been demonstrated that according to triboelectric series the electrification is the highest for Polyethyleneimine aqueous solution following heavy water and light water.
 - e. Nanofluids with conductive nanoparticles were used as strategy to further increase the electrification, and more than one order of magnitude enhancement of generated energy was achieved.
2. A high-pressure triboelectrification setup for intrusion-extrusion has been developed and tested under different configurations:
 - a. A double electrode active scheme with a non-zero bias voltage demonstrated the highest electrification results with figures of merits orders of magnitude higher compared to the state-of-the-art. However, bias voltage resulted in material degradation and slow kinetics of discharge.
 - b. A double electrode passive scheme with zero bias voltage demonstrated improved stability and kinetics, however, lower electrical energy generation.
 - c. A single electrode monolith configuration demonstrated both stable performance as well as reasonable electrification effects. This configuration possesses material challenge as it is difficult to produce a nanoporous monolith with porosity sufficient for the shock absorber prototype.
 - d. Effect of crystal size was found to have noticeable effect on the electrification, demonstrating that for smaller crystals the discharge kinetics is faster, while the generated energy is lower.
3. Effect of testing conditions was explored:
 - a. Bias voltage in a double electrode active scheme has a tremendous positive effect on the generated electricity. However, it has a negative effect on materials stability.
 - b. Compression-decompression rate was demonstrated to have proportional effect on the amplitude of generated current and voltage, while not affecting strongly the generated energy.
 - c. The generated energy is higher at higher temperature.
 - d. The optimum resistance for most of the configurations was found to be 10 – 20 kOhm.

The main theoretical activity aimed at identifying the contact electrification mechanism and can be summarized as follows:

1. Development of computational approaches for studying electronic contact electrification of defect-free and defected materials.
2. Crystalline porous systems, namely metal-organic frameworks (MOF)
 - a. Contact electrification of a defect-free MOF.
 - b. Contact electrification of MOFs containing defect.
 - c. Effect of intrusion on the formation of defects.
 - d. We concluded that defects are necessary for electronic contact electrification in the ideally perfect inner surface of crystalline porous materials to produce gap states that allow electron exchange between the two materials.
 - e. The expansion of the crystalline porous material lattice upon intrusion favours the formation of defects, resulting in positive feedback.
3. Grafted silica porous materials
 - a. Contact electrification of grafting defect-free grafted silica
 - b. Contact electrification grafted silica with grafting defects: electronic vs ionic electrification.
 - c. Effect of the type of grafting defects on the contact electrification.
 - d. It is concluded that grafting defects are necessary to allow electronic contact electrification. In particular, the defects resulting from heterolytic bond cleavage leaving on the silica a positive Si^+ defect both more likely to form and more efficient to produce contact electrification.
 - e. The relevance of grafting defects to allow contact electrification poses a challenge as the same defects make liquid extrusion more difficult.
4. Model monolithic system: grafting/silica/silicon
 - a. Contact electrification in a defect-free undoped grafting/silica/silicon system.
 - b. Contact electrification in a defect-free p-doped grafting/silica/silicon system.
 - c. Contact electrification in a grafting-defect undoped and doped grafting/silica/silicon system.
 - d. Results show that, concerning contact electrification, the grafting/silica/silicon system behave the same as grafted silica.

6. REFERENCES

1. Eroshenko, V. A., Piatiletov, I., Coiffard, L. & Stoudenets, V. A new paradigm of mechanical energy dissipation. Part 2: Experimental investigation and effectiveness of a novel car damper. *Proceedings of the Institution of Mechanical Engineers, Part D: Journal of Automobile Engineering* **221**, 301–312 (2007).
2. Li, X. *et al.* Solid–liquid triboelectrification control and antistatic materials design based on interface wettability control. *Adv Funct Mater* **29**, (2019).
3. Fadeev, A. Y. & Eroshenko, V. A. Study of penetration of water into hydrophobized porous silicas. *J Colloid Interface Sci* **187**, 275–282 (1997).
4. Amabili, M. *et al.* Pore morphology determines spontaneous liquid extrusion from nanopores. *ACS Nano* **13**, (2019).
5. Wu, H. *et al.* Controlled synthesis of highly stable zeolitic imidazolate framework-67 dodecahedra and their use towards the templated formation of a hollow Co₃O₄ catalyst for CO oxidation. *RSC Adv* **6**, 6915–6920 (2016).
6. Zhang, J., Zhang, T., Yu, D., Xiao, K. & Hong, Y. Transition from ZIF-L-Co to ZIF-67: a new insight into the structural evolution of zeolitic imidazolate frameworks (ZIFs) in aqueous systems. *CrystEngComm* **17**, 8212–8215 (2015).
7. Chen, R. *et al.* A two-dimensional zeolitic imidazolate framework with a cushion-shaped cavity for CO₂ adsorption. *Chemical Communications* **49**, 9500 (2013).
8. Grosu, Y. *et al.* Stability of zeolitic imidazolate frameworks: Effect of forced water intrusion and framework flexibility dynamics. *RSC Adv* **5**, 89498–89502 (2015).
9. Basset, P. *et al.* A batch-fabricated and electret-free silicon electrostatic vibration energy harvester. *Journal of Micromechanics and Microengineering* **19**, 115025 (2009).
10. Krupenkin, T. & Taylor, J. A. Reverse electrowetting as a new approach to high-power energy harvesting. *Nat Commun* **2**, 448 (2011).
11. Hsu, T.-H., Manakasettharn, S., Taylor, J. A. & Krupenkin, T. Bubbler: A Novel Ultra-High Power Density Energy Harvesting Method Based on Reverse Electrowetting. *Sci Rep* **5**, 16537 (2015).
12. Huynh, D. H. *et al.* Environmentally friendly power generator based on moving liquid dielectric and double layer effect. *Sci Rep* **6**, 26708 (2016).
13. Yang, H., Hong, S., Koo, B., Lee, D. & Kim, Y.-B. High-performance reverse electrowetting energy harvesting using atomic-layer-deposited dielectric film. *Nano Energy* **31**, 450–455 (2017).
14. Liu, W. *et al.* Integrated charge excitation triboelectric nanogenerator. *Nat Commun* **10**, 1426 (2019).
15. Adhikari, P. R., Tasneem, N. T., Reid, R. C. & Mahbub, I. Electrode and electrolyte configurations for low frequency motion energy harvesting based on reverse electrowetting. *Sci Rep* **11**, 5030 (2021).

16. Kim, D., Kim, D. Y., Shim, J. & Kim, K. C. Energy harvesting performance of an EDLC power generator based on pure water and glycerol mixture: analytical modelling and experimental validation. *Sci Rep* **11**, 23426 (2021).
17. Wang, Z. L. & Wang, A. C. On the origin of contact-electrification. *Materials Today* **30**, 34–51 (2019).
18. Xu, C. *et al.* Contact-electrification between two identical materials: Curvature effect. *ACS Nano* **13**, acsnano.8b08533 (2019).
19. Lin, S., Xu, L., Chi Wang, A. & Wang, Z. L. Quantifying electron-transfer in liquid-solid contact electrification and the formation of electric double-layer. *Nat Commun* **11**, 399 (2020).
20. Willatzen, M. & Lin Wang, Z. Theory of contact electrification: Optical transitions in two-level systems. *Nano Energy* **52**, 517–523 (2018).
21. Xu, C. *et al.* On the Electron-Transfer Mechanism in the Contact-Electrification Effect. *Advanced Materials* **30**, (2018).
22. Grosu, Y. *et al.* Mechanical, thermal, and electrical energy storage in a single working body: Electrification and thermal effects upon pressure-induced water intrusion–extrusion in nanoporous solids. *ACS Appl Mater Interfaces* **9**, 7044–7049 (2017).
23. Tortora, M. *et al.* Giant negative compressibility by liquid intrusion into superhydrophobic flexible nanoporous frameworks. *Nano Lett* **21**, 2848–2853 (2021).
24. Bader, R. F. W. Atoms in molecules. *Acc Chem Res* **18**, 9–15 (1985).
25. Zhang, C., Han, C., Sholl, D. S. & Schmidt, J. R. Computational characterization of defects in Metal–Organic Frameworks: Spontaneous and water-induced point defects in ZIF-8. *J Phys Chem Lett* **7**, 459–464 (2016).
26. Löwdin, P.-O. On the non-orthogonality problem connected with the use of atomic wave functions in the theory of molecules and crystals. *J Chem Phys* **18**, 365–375 (1950).
27. Lin, S., Zheng, M., Luo, J. & Wang, Z. L. Effects of surface functional groups on electron transfer at liquid–solid interfacial contact electrification. *ACS Nano* **14**, 10733–10741 (2020).
28. Emami, F. S. *et al.* Force field and a surface model database for silica to simulate Interfacial properties in atomic resolution. *Chemistry of Materials* **26**, 2647–2658 (2014).
29. Jorgensen, W. L. & Tirado-Rives, J. Potential energy functions for atomic-level simulations of water and organic and biomolecular systems. *Proceedings of the National Academy of Sciences* **102**, 6665–6670 (2005).
30. Dodda, L. S., Vilseck, J. Z., Tirado-Rives, J. & Jorgensen, W. L. 1.14*CM1A-LBCC: Localized bond-charge corrected CM1A charges for condensed-phase simulations. *J Phys Chem B* **121**, 3864–3870 (2017).
31. Dodda, L. S., Cabeza de Vaca, I., Tirado-Rives, J. & Jorgensen, W. L. LigParGen web server: an automatic OPLS-AA parameter generator for organic ligands. *Nucleic Acids Res* **45**, W331–W336 (2017).
32. Geissler, P. L., Dellago, C., Chandler, D., Hutter, J. & Parrinello, M. Autoionization in liquid water. *Science (1979)* **291**, 2121–2124 (2001).

